Alteration conditions on the CM and CV parent bodies – Insights from hydrothermal experiments with the CO chondrite Kainsaz

Journal Item

Available online at www.sciencedirect.com

ScienceDirect

Geochimica et Cosmochimica Acta 318 (2022) 83–111

Geochimica et Cosmochimica Acta

www.elsevier.com/locate/gca

Alteration conditions on the CM and CV parent bodies – Insights from hydrothermal experiments with the CO chondrite Kainsaz

M.D. Suttle [a,b,*], A.J. King [a], N.K. Ramkissoon [b], E. Bonato [a,c], I.A. Franchi [b], J. Malley [b], P.F. Schofield [a], J. Najorka [d], T. Salge [d], S.S. Russell [a]

[a] *Planetary Materials Group, Department of Earth Sciences, Natural History Museum, Cromwell Road, London SW7 5BD, UK*
[b] *Faculty of Science, Technology, Engineering and Mathematics, The Open University, Walton Hall, Milton Keynes MK7 6AA, UK*
[c] *Institute of Planetary Research, German Aerospace Center (DLR), Berlin, Germany*
[d] *Imaging and Analysis Centre, Natural History Museum, Cromwell Road, London SW7 5BD, UK*

Received 29 August 2021; accepted in revised form 26 November 2021; Available online 3 December 2021

Abstract

This study simulates the hydrothermal conditions that existed on carbonaceous chondrite planetesimals in the early solar system. Our experiments are relevant to alteration conditions that existed on the CV parent body and the late stage oxidizing alteration of the CM chondrites. We conducted 11 alteration experiments using chips of the CO3 chondrite Kainsaz. Water was added to each chip and sealed in separate Teflon reaction vessels for 175 days. Samples were altered at different initial water-to-rock ratios (W/R: 0.2–0.8) and temperatures (50 °C and 150 °C). Isotopically doped ^{17}O-rich heavy water ($\delta^{17}O$: +64.5‰) was used in five runs. All samples experienced pronounced alteration under a partially open system environment where gases were able to escape the reaction vessels.

The style of alteration (Fe-alkali metasomatism) is similar in all cases. The principal alteration minerals formed are Fe-oxyhydroxides (goethite) and Fe-oxides (magnetite), with smaller quantities of Fe-sulphides. Minor phases formed include fayalite, sulphates (gypsum and Fe-sulphate) and calcite. Nanophase, poorly crystalline phyllosilicates formed in the high-temperature samples but are absent from the low-temperature experiments. In all instances, Mg-rich chondrule silicates remained chemically unaltered although some grains suffered hydrothermal fracture. Chondrule mesostases remained largely unaffected. By contrast, kamacite readily dissolved, acting as a source of Fe and Ni for the fluid phase. A new generation of nanophase Fe-sulphides formed within the matrix, while pre-existing pyrrhotite group sulphides experienced Ni enrichment (<3 at%). In the high temperature samples these sulphides were also partially oxidized, lowering their (Fe + Ni)/S ratio. High-Ni sulphides (pyrrhotite with Ni > 10 at%) were formed in the 150 °C samples, most likely by sulphidation of taenite.

Matrix alteration cemented grains together, reducing porosity. The fine-grained matrix shows highly variable degrees of alteration, with minimally altered matrix in direct contact with regions of heavily altered matrix. Chondrule fine-grained rims (FGRs) were preferentially altered. These textures imply that the unaltered matrix readily reacted with the fluid phase, resulting in an efficient depletion of dissolved ions (Fe^{2+} and S^{2-}), limiting reactivity until further primary phases were dissolved. At larger length-scales the distribution of heavily altered matrix reveals the presence of large ~100 μm wide channels that meander through the specimens. Their textures resemble features seen in some CM chondrites and the ungrouped CO-like

* Corresponding author at: Planetary Materials Group, Department of Earth Sciences, Natural History Museum, Cromwell Road, London SW7 5BD, UK.

E-mail addresses: martin.suttle@open.ac.uk (M.D. Suttle), a.king@nhm.ac.uk (A.J. King), nisha.ramkissoon@open.ac.uk (N.K. Ramkissoon), enrica.bonato@dlr.de (E. Bonato), ian.franchi@open.ac.uk (I.A. Franchi), james.malley@open.ac.uk (J. Malley), p.schofield@nhm.ac.uk (P.F. Schofield), j.najorka@nhm.ac.uk (J. Najorka), t.salge@nhm.ac.uk (T. Salge), sara.russell@nhm.ac.uk (S.S. Russell).

https://doi.org/10.1016/j.gca.2021.11.028

chondrite MIL 07687. We suggest that alteration fronts developed by sustained rapid reaction of matrix with dissolved cations in solution. Our observations provide a mechanism for the establishment and maintenance of geochemical microenvironments on chondritic asteroids. The effects of open system loss notwithstanding, our experiments demonstrate that more advanced alteration is correlated with higher initial W/R ratios.

The use of ^{17}O-rich doped water allowed the isotopic effects of aqueous alteration to be observed. Bulk rock compositions evolved towards the initial water composition, reflecting the incorporation of heavy O into hydrated minerals. Additionally, altered samples shifted in δ^{18}O space, reflecting the competing effects of water–mineral fractionation and mass fractionation due to the preferential escape of isotopically light water.

Keywords: Carbonaceous chondrites; Aqueous alteration; Water-to-rock ratios; Open system; Experimental

1. INTRODUCTION

Shortly after the formation of refractory Ca-, Al-rich inclusions (CAIs) and chondrules large planetesimals with diameters >100 km accreted (e.g. Shukolyukov and Lugmair, 2002; Krot et al. 2006; Edwards and Blackburn, 2020). The stable isotope compositions (e.g. ε^{54}Cr, ε^{50}Ti and ε^{58}Ni) of meteorites (derived from these bodies [Greenwood et al. 2020]) and of terrestrial planets provides compelling evidence for a first-order dichotomy in solar system materials, separating objects into carbonaceous chondrite (CC) and non-carbonaceous chondrite (NC) groupings (Warren, 2011; Nanne et al. 2019). This division most likely represents the segregation of the solar system into inner and outer regions, facilitated by the rapid formation of Jupiter (e.g. Nanne et al. 2019; Kleine et al. 2020). The study of CC meteorites therefore provides an opportunity to investigate the geological diversity and complex petrographic evolution of volatile-rich outer solar system planetesimals.

Extinct short-lived radiochronometers such as the ^{53}Mn-^{53}Cr system indicate that the onset of geological activity on CC planetesimals occurred between 1–5 Ma after CAI formation and continued for up to 15 Ma (Krot et al. 2006; Fujiya et al. 2012; Doyle et al. 2015; Jogo et al. 2017; Visser et al. 2020). Carbonaceous chondrites record a wide range of alteration environments characterised by extensive fluid-rock interaction and the formation of new secondary mineral assemblages. They define a continuous spectrum between aqueous alteration operating at low-temperatures and relatively high water-to-rock (W/R) ratios through to thermal metasomatism operating at higher temperatures and lower W/R ratios (Young, 2001; Krot et al. 2006; Brearley, 2006; Brearley and Krot, 2013; Marrocchi et al., 2018; Suttle et al. 2021a).

The three most abundant CC subgroups are the COs (>680 meteorites), the CMs (>710 meteorites) and the CV chondrites (>600 meteorites) (The Meteoritical Bulletin, 2021). Together they represent approximately 70% of all carbonaceous chondrites. The CM chondrites are dominated by phyllosilicates and contain hydrated sulphides as well as magnetite, carbonate (Browning et al. 1996; Rubin et al. 2007; Howard et al., 2009; 2011; 2015) and limited quantities of ferrihydrite and goethite (Pignatelli et al. 2017). They record extensive interaction with liquid water at relatively low temperatures. Multiple studies have investigated the CM chondrites and concluded that temperatures during alteration were most likely between 20 °C-200 °C and initial W/R ratios between 0.2 and 0.7 (summarized in Suttle et al. [2021a]). Investigation of different generations of carbonate found in CM chondrites reveals that alteration operated on a prograde path (increasing temperature with time) (Vacher et al. 2019a) and was potentially episodic in nature (Lee et al., 2012; 2014). Based on the presence of sodalite in the minimally altered CM MET 01075 Lee et al. (2019a) suggested that a short-lived episode of alkali metasomatism may have affected the CMs chondrites prior to aqueous alteration.

The CV chondrites are composed of anhydrous Fe-Mg-Ca silicates (olivine and pyroxene), amphiboles, feldspars (anorthite), nepheline, magnetite, Fe-Ni-sulphides and rare Fe-Ni-metal with minor quantities of phyllosilicates and Fe-oxides in some samples (McSween, 1977a; Howard et al. 2010; MacPherson and Krot, 2014). The main alteration minerals are Fe-rich olivine (fayalite), Fe-Ca-rich pyroxenes and magnetite (Hua and Buseck, 1995; Krot et al. 1998; MacPherson and Krot 2014). As a result, alteration conditions on CV chondrites are classed as Fe-alkali-halogen metasomatism, reflecting the main elements that were mobilized during alteration (Brearley and Krot, 2013). The CV chondrites are divided into two main subgroups (oxidized [CV_{ox}] and reduced [CV_{Red}]) based on their bulk mineralogy and presence of magnetite. These subgroupings are interpreted as different alteration environments (potentially on different parent asteroids [Bonal et al. 2020; Gattacceca et al. 2020]). Despite this division, alteration styles for the CV lithologies can be generalized and, relative to the CM chondrites, they appear to have been altered at lower initial W/R ratios (0.06–0.2, Zolotov et al. [2006], 0.07–0.18, Jogo et al. [2009], 0.1–0.2, Marrocchi et al. [2018]) and possibly at higher temperatures (<350 °C, Zolotov et al. 2006; Jogo et al. 2009, 210–610 °C, Ganino and Libourel, 2017). A more recent survey of secondary mineralogy argued that the division of CV chondrites should be based on their secondary Ca-Fe-rich silicates and split into either andradite-bearing (CV_{OX}) or kirschsteinite-bearing (CV_{Red}) (Ganino and Libourel, 2017). It is proposed that CV alteration occurred under reducing conditions (approximately the iron-magnetite buffer) and was governed primarily by silica activity. Investigation of naturally formed terrestrial samples indicates that CV alteration may have occurred by rock-vapour interac-

tions under conditions similar to fumarole settings on Earth (Ganino and Libourel, 2020).

The CO chondrites share similarities with both the CM and CV chondrites. Chemically, isotopically and texturally they are closely related to the CM chondrites (Kallemeyn and Wasson, 1981; Rubin and Wasson, 1986; Clayton and Mayeda, 1999; Weisberg et al., 2006; Kimura et al. 2020; Torrano et al. 2021; Zhu et al. 2021). However, unlike the CM chondrites, the CO chondrites experienced minimal aqueous alteration (Marrocchi et al., 2018; Alexander et al., 2018). Instead, they record thermal metamorphism under conditions similar to the CV chondrites, but less-extreme (Brearley and Krot, 2013). The COs display a petrologic sequence from pristine CO3.0 s to altered CO3.7 s (McSween, 1977b; Sears et al., 1991; Bonato, 2020). Similarities between the CO and CM chondrites are so striking that the two subgroups are sometimes referred to as the CO-CM clan (Weisberg et al. 2006). Studies have suggested that they originated from a single parent body (Kallemeyn and Wasson, 1981) while more recent works favour a model in which the two groups existed as asteroidal neighbours in the protoplanetary disk (Schrader and Davidson, 2017; Chaumard et al., 2018; Kimura et al. 2020). In either case the CO and CM chondrites accreted similar primary materials, with the main difference being that the CMs accreted proportionally more water–ice, leading to high initial W/R ratios (Chaumard et al., 2018). This difference was therefore probably responsible for their divergent alteration histories.

Recently Kimura et al. (2020) described three highly primitive CM chondrites containing minimal phyllosilicates as well as intact chondrules glass, pristine metal and sulphides and melilite-bearing CAIs. They proposed that one of these meteorites (Asuka [A] 12169) should be classified as an unaltered CM3 chondrite. The matrix in A 12169 is dominated by amorphous phases with properties similar to the GEMS (glass with embedded metal and sulphides) phases found in cometary dust (Bradley, 1994; 2019; Noguchi et al., 2015). Also present are condensation-crystallized anhydrous phases such as enstatite whiskers. Asuka 12169 bears close similarities to the most primitive CO chondrites, notably the CO3.00 DOM 08006 (Davidson et al. 2019; Alexander et al. 2018) in terms of its refectory inclusion chemistry, O-isotopy and critically in its matrix mineralogy.

In this work we explore the relationship between the CO and CM chondrites further by testing if aqueous alteration of a minimally altered CO chondrite will produce a CM-like lithology. Our experiments are therefore designed to test if CO chondrites are a reasonable analogue for the unaltered CM3 precursor material and therefore if CO-CM clan could have originated from a single parent body. Understanding how chondrite groups are related as well as their primordial accretionary properties are important science goals because this information will help us to better resolve the structure of the protoplanetary disk and the process of planet formation.

We conducted a series of hydrothermal alteration experiments using chips of the CO3.2 chondrite Kainsaz as the starting material. Experimental variables aimed to reconstruct conditions on the CM parent body during aqueous alteration (Suttle et al. 2021a). We selected temperature (50 °C and 150 °C) and initial W/R ratios (0.2–0.8) as the main variables (Table 1) and used isotopically doped ^{17}O-rich water in some experiments. Additionally, this study provides insights into how open system behaviour influences aqueous alteration. The experimental products were analysed using a combination of scanning electron microscopy (SEM), energy-dispersive spectrometry (EDS), infrared (IR) spectroscopy, X-ray diffraction (XRD), thermogravimetric analysis (TGA) and bulk oxygen isotope mass spectrometry.

2. PREVIOUS EXPERIMENTAL AQUEOUS ALTERATION STUDIES

Most research into aqueous alteration on chondrite parent bodies takes the form of descriptive investigation using microanalysis techniques to study naturally altered meteorites. In contrast there are relatively few studies which employ an experimental approach. However, when applied experimental studies often use synthetic starting materials. Amorphous Fe-Mg-silicate "smokes" are one such example, they approximate the composition and structure of the main phases found in the matrices of primitive chondritic materials – these are referred to as GEMS when present in cometary dust (Bradley, 1994; 2019; Noguchi et al., 2015) or GEMS-like phases when found in carbonaceous chondrites and fine-grained micrometeorites (Le Guillou et al. 2015; Leroux et al., 2015; Suttle et al. 2021b). The aqueous alteration of amorphous smokes occurs rapidly (<48 hours), even at low temperatures (<25 °C). Their hydration forms simple phyllosilicates such as Fe and Mg bearing serpentine (Nelson et al., 1987; Rietmeijer et al., 2004; Nakamura-Messenger et al. 2011; Takigawa et al., 2019). Experimental studies have successfully produced characteristic CM chondrite minerals from synthetic starting materials. Peng and Jing (2014) exposed alloyed metal particle mixtures to reducing, alkaline S-bearing fluids and generated a diversity of CM-like minerals including tochilinite, cronstedtite and intergrown mixtures of these minerals as well as polyhedral serpentine. More recently, Vacher et al., (2019b) used a powdered mixture of Mg-Fe-smokes, Fe-metal and San Carlos olivine sealed in glass vessels with W/R ratios of 10 and heated to 80 °C for 30–60 days, resulting in Mg-bearing tochilinite and triangular cronstedtite crystals. They concluded that CM alteration operated under low temperature reducing conditions while variable S activities were required to form the characteristic tochilinite cronstedtite intergrowth (TCIs) textures found in CM chondrites. Recently, Kikuchi et al. (2021) used a mix of forsterite, enstatite, silicate glass, troilite and metal. They simulated hydrothermal alteration on generic carbonaceous chondrite asteroids at low temperatures (25–80 °C), high W/R ratios (10) and long durations (<460 days). The resulting assemblages produced pyrrhotite, amorphous SiO_2-bearing phases and saponite (but no serpentine).

Alternatively, some studies focus on the alteration of crystalline silicates. They generally explore how environmental variables control the dissolution and replacement

Table 1
Experimental variables and estimated environmental conditions for the 11 samples investigated in this study (A-E, K-O & Q). Also included are mass increase data measurements collected shortly after the reaction vessels were opened. The final column shows the estimated percentage of unreacted water, this could be either water that was lost from the reaction vessel during the experiment due to (unplanned) open system behaviour or where water remained at the end of the experiment (as in samples C, D & E). *Note sample Q was powdered while all other samples were reacted as whole rock chips.

Sample	Temp. (°C)	W/R_E	Heavy water?	Duration (days)	Estimated pressure (bar)	Mass percent increase (%)	Residual water at termination	Est. percent water unreacted (%)
A	50	0.2		175	1.12	7.7		62
B	50	0.4		175	1.12	2.6		93
C	50	0.6		175	1.12	24.1	Y	60
D	50	0.8	Y	175	1.12	28.3	Y	65
E	50	0.8	Y	175	1.12	7.8	Y	90
K	150	0.2		175	4.78	2.3		88
L	150	0.4		175	4.78	4.6		88
M	150	0.6		175	4.78	5.4		91
N	150	0.8	Y	175	4.78	5.5		93
O	150	0.8	Y	175	4.78	6.2		92
Q*	150	0.8	Y	170	4.78	*No data*		*No data*

of pure olivine and pyroxene (Ohnishi and Tomeoka, 2007; Lamadrid et al., 2017). Such studies are of interest to both meteoritics and terrestrial geology, and their reaction dynamics are well-constrained. Olivine alters to serpentine and brucite in the following reaction:

$$2Mg_2SiO_4(Ol.) + 3H_2O \rightleftharpoons Mg_3Si_2O_5(OH)_4(\text{Serp.}) + Mg(OH)_2(\text{Bruc.}) \quad (1)$$

where Fe is present within olivine's composition, secondary magnetite may also form:

$$3Fe^{2+} + 4H_2O \rightleftharpoons Fe_3O_4 + H_2 + 6H^+ \quad (2)$$

These reactions consume water, thereby lowering the system's W/R ratio and leading to a proportional increase in the concentration of dissolved ions (increasing the system's salinity). Lamadrid et al., (2017) demonstrated that reaction rates are heavily dependent on salinity. As the availability of water decreases, reaction rates slow. In terrestrial settings, open system behaviour and water circulation, where high salinity water can be replaced by lower salinity water (e.g. in the alteration basalt pillow lavas on the seafloor) is critical for achieving complete serpentinization. Conversely, in chondritic settings, where the supply of water is expected to have been finite, initial W/R ratios (controlled by the accretion of water–ice) combined with the later potential loss of water (for example, degassing into space [Young et al., 1999]) are expected to have played a major role in defining the extent of aqueous alteration (Clayton and Mayeda, 1999).

Very few studies have used natural meteorite samples as starting materials for experimental hydration. Jones and Brearley (2006) altered the CV chondrite Allende under oxidising conditions, at temperatures between 100 °C and 200 °C with W/R ratios between 1 and 9 and over variable timescales (7–180 days). They concluded that Ca and Mg ions are rapidly mobilized and form soluble salts (calcite, gypsum and epsomite) which were deposited on the external surface of the altered chips alongside abundant Fe-oxides and Fe-hydroxides. Crucially, the extent of alteration was strongly correlated with W/R ratio but less dependent on alteration duration. Furthermore, they argued that the coarse grain size of their hydrated products suggested that aqueous alteration on asteroids proceeded at lower temperatures than those investigated.

The isotopic effects of aqueous alteration have also been investigated. Ivanova et al., (2013) altered olivine mineral standards with isotopically doped heavy water. They achieved increases of + 10‰ in the $\delta^{18}O$ composition of the resulting phyllosilicates (while a later dehydration experiment further raised $\delta^{18}O$ values by + 7‰). These experiments aimed to produce heavy isotopic signatures similar to those measured in the Belgica-like meteorites (which are now recognised as their own distinct meteorite group, the CY chondrites [King et al., 2019]). The use of isotopically doped water provides an additional perspective to alteration studies, tracing how the fluid and rock have interacted at the atomic level.

3. METHODS AND EXPERIMENTAL DESIGN

3.1. Choice of starting material

We selected the meteorite Kainsaz as our starting material. This is a CO3.2 chondrite that is well characterised by previous studies (e.g. Rubin et al., 1985; Keller and Buseck, 1990; Bonato, 2020). Matrix comprises approximately 30 vol% and is composed primarily of small olivine and pyroxene grains (Ahrens et al. 1973). Chondrules are predominantly porphyritic olivine-pyroxene (POP) varieties. CAIs are relatively rare (~0.7 vol%, Russell et al. 1998), while amoeboid olivine aggregates (AOAs) are more abundant (~4.4 vol%, Ebel et al. 2016). Modal mineralogy was

previously calculated by Bonato (2020): olivine (48.7 vol%), pyroxene (40.8 vol%), Fe-Ni-metal (1.3 vol%), Ca-rich feldspar (4.2 vol%) and Fe-Sulphides (5.0 vol%), with no magnetite detected. The bulk O-isotope composition of Kainsaz exhibits minimal variability. Previous analysis by Clayton and Mayeda (1999) produced values of $\delta^{17}O$: −5.68‰, $\delta^{18}O$: −1.85‰ and $\Delta^{17}O$: −4.71‰, while Alexander et al., (2018) published values of: $\delta^{17}O$: −6.60 ± 0.03‰ (1σ), $\delta^{18}O$: −2.61 ± 0.01‰ (1σ) and $\Delta^{17}O$: −5.24 ± 0.03‰ (1σ) (Table 2). A key factor in our choice of starting material was the relatively large quantity of Kainsaz available for study, with an initial recovered mass of ∼ 200 kg (The Meteoritical Bulletin, 2021). It is also the least metamorphosed CO chondrite fall (Bonato, 2020), meaning that its mineralogy, textures and isotopic composition are relatively unaffected by terrestrial alteration (weathering) and only partially affected by parent body metamorphism. Furthermore, CO chondrites are considered nominally anhydrous having experienced minimal contact with liquid water whilst on their parent body (Marrocchi et al., 2018; Alexander et al., 2018). As a result, Kainsaz represents a suitable approximation of the anhydrous CM3 protolith (Rubin, 2015; Kimura et al., 2020) and an adequate choice of starting material in our attempts to reproduce a CM-like alteration assemblage.

3.2. Selection of environmental variables

We opted to use meteorite chips (as opposed to powdered samples) as the starting materials. This ensured that the spatial relationships between reactants and products could be investigated using a SEM after the experiments were concluded. One exception to this was sample Q which was powdered to test if a larger exposed surface area affected alteration extent. The selection of temperature range and W/R ratios was informed by previous literature estimates for the aqueous alteration conditions on the CM and CV parent bodies. By selecting 50 °C and 150 °C, we could investigate low and higher temperature conditions relevant to both the CM and CV chondrites. Likewise, we selected initial W/R ratios between 0.2 and 0.8 (stepped in intervals of 0.2), covering the entire spread estimated from previous literature for both the CMs (Suttle et al., 2021a) and CVs (Zolotov et al. 2006; Jogo et al. 2009; Marrocchi et al. 2018). Initially we planned to also investigate the duration of alteration, however, owing to the disruption to research caused by the COVID-19 global pandemic and associated shutdown of laboratories we did not terminate the hydration experiments in two separate batches (as initially planned) but instead ended all the experiments at the same time (this resulted in two experimental runs conducted at the same W/R ratio [0.8] in each temperature batch).

3.3. Hydration experiments

A single chip (∼1.2 g) of Kainsaz was acquired from the Natural History Museum (NHM), London. The chip was extracted from a larger specimen, BM1972, 232. It was subsequently crushed using a hammer and chisel to produce a series of smaller fragments with a range of sizes, shapes and masses. Each experimental run used either a single chip or two chips with a (combined) dry mass of at least 85 mg (ranging from 85-157 mg, with a mean average of 113 mg).

We used sealed reaction vessels composed of a stainless-steel outer shell that holds an inner Teflon container with a volume of 10 ml. These reaction vessels are sold by VWR as Parr Acid Digestion Vessels (model No. 4749A) and are designed to withstand temperatures up to 250 °C and pressures up to 124 bar. Where pressures exceed the stated maximum, the vessels are designed to safely release excess gas effusively (avoiding explosive behaviour). In our experiments estimated pressures range from 1.12 bar for the low-temperature samples and 4.78 bar for the high-temperature samples (Table 1)[1]. Both values are well below the stated pressure limit of the reaction vessels.

We conducted 11 hydration experiments, each in their own separate reaction vessel. The specified dry mass of CO chondrite was added to the vessel (given in Table 1) and then, using a micro-litre pipette the required quantity of water added. The amount of water to be added was defined by the W/R (mass) ratio being tested. This varied between 0.2 and 0.8 (in increments of 0.2). We used either deionised milli-Q water or isotopically doped ^{17}O-rich water. However, because the amount of isotopically doped water available was limited, only some experiments were reacted with heavy water. The headspace in each reaction vessel (<10 ml) was atmospheric air. Reaction vessels were then sealed and left static in either a 50 °C or a 150 °C laboratory oven for 170–175 days (Table 1). The vessels were then removed from their oven and allowed to cool overnight to room temperature before being opened. At the end of each experiment the rock chips (once dry) were weighed (Table 1). The time between removal from the oven to opening (and if required drying) took < 24 hours.

3.4. Post experiment sample preparation and analysis

All analytical techniques were performed at the Natural History Museum (London), with the exception of the O-isotope measurements which were conducted at the Open University.

After terminating the hydrothermal alteration experiments, the altered rock chips were processed for analysis. For every sample we retained a small chip that was prepared for 2D *in-situ* analysis. These chips were embedded in epoxy resin, sectioned, polished and carbon coated. They were then investigated under SEM (a Zeiss EVO LS15) using backscattered electron (BSE) imaging, point EDS and large-area EDS mapping to study textures, mineral

[1] Note chamber pressures in the low-temperature samples are solely a product of thermal expansion of the air held inside the container, this is because all the water remains liquid at temperatures of 50°C. Conversely, the high-temperature samples have elevated pressures arising due to the formation of steam. Conditions are such that in all the 150°C samples a mix of water and steam are predicted. Pressures were therefore held at the equilibrium saturation curve for the given pressure/temperature conditions. Steam tables show this to be 4.78 bar [Haar, 1984].

Table.2
Measured bulk O-isotope compositions for the samples (D, E, N, O & Q) reacted with isotopically doped ^{17}O-rich heavy water. Also shown are the unaltered Kainsaz composition (literature values) and the isotopically doped ^{17}O-rich heavy water composition. Note the "-" symbol denotes where literature data did not include associated uncertainty values.

Sample	Temp (°C)	W/R_E	Mass (mg)	O2 (µg)	Yield (%)	$\delta^{17}O$	2 σ	$\delta^{18}O$	2 σ	$\Delta^{17}O$	2 σ	Reference
Unaltered Kainsaz			N/A			-5.68	-	-1.85	-	-4.72	-	Clayton & Mayeda, 1999
						-6.60	0.06	-2.61	<0.01	-5.24	0.06	Alexander et al. 2018
Heavy water						64.49	-	-3.92	-	66.53	-	Morris, 2008
Sample D	50	0.8	2.66	758	28.5	7.62	0.05	-1.50	0.02	8.40	0.06	
Sample E	50	0.8	2.52	607	24.1	-0.71	0.05	-3.71	0.02	1.22	0.05	
sample N	150	0.8	2.51	717	28.5	12.04	0.03	0.80	0.01	11.62	0.03	*This study*
Sample O	150	0.8	2.53	896	35.4	11.51	0.05	0.54	0.01	11.23	0.05	
sample Q	150	0.8	2.52	697	27.7	5.35	0.03	-0.64	0.02	5.68	0.03	

associations and mineral compositions. The EDS system was an Oxford Instruments XMax 80 mm^2 silicon drift detector running the Aztec software. Mineral chemistry and matrix analyses were collected under high vacuum and employed an accelerating voltage of 20 kV, a monitored beam current of 1.5nA and a fixed working distance of 10 mm. We used the "*O by stoichiometry*" quantification routine for the analysis of silicates, "*C by difference*" for the analysis of carbonates and the "*all elements*" quantification routine for the investigation of oxides, sulphides and metals.

After SEM analysis, carbon coats were removed, and their flat exposed surfaces investigated using IR spectroscopy using a Thermo Nicolet iN10 reflectance microscope to infer the mineralogy of their fine-grained matrices. We used a 50x50µm beam footprint and each spectrum combined 120 scans with a 4 cm^{-1} spectral resolution. A reference background spectrum (collected upon a gold standard) was subtracted from the raw data. Data were collected in air with standard atmospheric corrections applied using the native OMNIC software.

The remaining experimental products (a rock chip between 60–100 mg from each experiment) were crushed to form powders for investigation by bulk analysis techniques (XRD, TGA and, on some fragments O-isotope mass spectrometry). Each powder was first analysed by XRD for qualitative mineral identification using a high-resolution Co-source Panalytical Scanning Diffractometer (X'Pert Pro MPD). We then performed quantitative phase analysis (QPA) XRD to determine each sample's modal mineralogy. This was achieved using a Cu-source ENRAF Nonius FR 590 X-ray diffractometer fitted with a curved 120° position sensitive detector. Analysis protocol followed those outlined in Cressey and Schofield (1996), Schofield et al. (2002), Howard et al., (2009; 2011; 2015) and King et al., (2019). After XRD a small aliquot (~10 mg) of powder was studied by TGA (using a TA Instruments SDT Q600 TGA instrument) to determine volatile contents. The TGA system heats a powdered sample in a N_2 laminar flow atmosphere (~100 ml min^{-1}) at a rate of + 10 °C mi n^{-1}, from room temperature (~25 °C) to 1000 °C. The sensitivity of the TGA balance is 0.1 µg and the overall error on the measured mass loss fractions is ~ 0.1%.

Finally, a small quantity of (unheated) powder (~1–2 mg) from each of the five experiments reacted with doped water (Sample D, E, N, O and Q) were directed for triple O-isotope mass spectrometry using the Open University's laser fluorination line. Because the altered CO chondrite samples contained hydrated phases, we were cautious to avoid any potential pre-reaction between hydrated alteration phases in the sample with the BrF_5 gas during the blank reduction procedure. As a result all five altered samples were analysed using the "single shot" protocol. Full details of this technique are outlined in Lee et al. (2019b).

3.5. Geochemical modelling

The thermochemical modelling code CHIM-XPT (Reed et al., 2010) was used to identify possible reaction pathways. CHIM-XPT has previously been used to explore water–rock interactions in terrestrial (e.g. Palandri and Reed, 2004; Reed, 1983) and Martian settings (e.g. Bridges et al., 2015; Filiberto and Schwenzer, 2013; Schwenzer and Kring, 2013). The code applies mass balance and mass action equations to compute heterogenous multicomponent chemical equilibria of solids, aqueous and gas phases (Reed, 1982). The Soltherm thermodynamic database was used for these models. This database is an adapted version of the slop07.dat database (available at http://geopig.asu.edu/sites/default/files/) that has been merged with mineral and gas properties from Holland and Powell (2011).

The model assumes the complete dissolution of rock within fluids, which means that modelled water–rock ratios (hereafter denoted by a subscript M: W/R_M) refers to only the amount of rock that reacted with fluids in the geochemical model. By contrast, when referring to the initial W/R ratios in our experiments (hereafter denoted by a subscript E: W/R_E) we mean the amount (by mass) of rock and water added at the start of each experiment. Therefore, the W/R_M would reflect the amount of rock that reacted within the alteration experiments. The use of two different uses of W/R ratio follow the practice given in Olsson-Francis et al. (2017) and aims to provide a more effective means of discussing aqueous alteration reactions.

In our geochemical model stepwise titrations were conducted from a high W/R_M of 100,000 to a low W/R_M of 1 in order to assess how the secondary mineral assemblage varies as alteration progresses. Pure H_2O was used as the starting fluid, and iterative modelling was used to determine the initial composition of reacted rock. Experimental results showed limited alteration of olivine chondrules, therefore, olivine was systematically removed from the bulk meteorite composition until suitable secondary mineral assemblages were achieved, which resulted in a model input composition that differed to the overall bulk compositions (Table 3). Models were run at temperatures of 50 °C and 150 °C and pressure of 1.0 and 4.7 bars, respectively. The pH was treated as a free parameter and the Cl anion was used for charge balance.

4. RESULTS

4.1. Initial observations at experiment termination

Upon opening the reaction vessels only three samples still retained visible water (Table 1, Fig. S1), all of which were low-temperature (50 °C) experiments (samples C, D and E). Visual inspection showed that sample E retained the most water. However, in all cases the quantity of water remaining was small, appearing as a film that coated each chip's surface. This water could not be extracted for wet chemical analyses and was instead allowed to dry in the low humidity environment of the clean laboratory, leaving behind the dry altered meteorite chips. All samples also left an orange-brown stain where the rock had been in contact with the surface of the Teflon reaction vessel (Fig. S1), suggestive of Fe-oxyhydroxide/oxide formation.

Additionally, all experiments showed an increase in mass, ranging from + 2.3% to + 28.3% (Fig. S2). Among the low-temperature (50 °C) experiments three samples (A, C and D) appear to have undergone significant alteration with notable increases in mass observed. Taken together, these three points define a polynomial trendline revealing a non-linear positive correlation between higher W/R_E ratios and larger mass increases (note, these trendlines have a pre-defined fixed intercept at the origin). By contrast, the remaining two low-temperature runs (B and E) show only modest mass increases (+2.6% and + 7.8% respectively) relative to their starting W/R_E ratio and do not follow the same trend defined by the other low-temperature samples (A, C and D). Among the high-temperature (150 °C) experiments, all five chips (K-O) appear to have behaved similarly. They define a separate polynomial trendline with a positive correlation, however, in these runs increasing W/R_E ratio appears to have had only a slight effect on the final mass, with none of the 150 °C samples increasing by more than + 6.2%. If the mass increase at the end of the experiments is taken simply as a metric of alteration extent, these data imply that the low-temperature samples are, on average more altered than the high-temperature samples.

Table.3
Host rock compositions used in our geochemical modelling. ([a]Rubin et al. [1985], [b]Brearley and Jones [2018]).

	Kainsaz bulk composition[a] (Wt%)	Model input* (Wt%)
SiO_2	34.68	4.67
TiO_2	0.22	0.61
Al_2O_3	3.72	10.39
Fe_2O_3	0.00	0.00
FeO	7.37	0.00
MnO	0.30	0.84
MgO	24.72	0.00
CaO	2.50	6.98
Na_2O	2.46	6.87
K_2O	0.20	0.56
P_2O_5	0.18	0.50
Fe(m)	18.36	51.26
Ni	1.65	4.61
FeS	4.15	11.59
C	0.38	1.06
Cl[b]	0.03	0.07
Total	101.64	100.0

* Data has been renormalised to a wt% of 100.

4.2. The unaltered Kainsaz

For clarity we describe observations on the unaltered Kainsaz first and then in the subsequent sections (4.3 to 4.7) detail observations from the altered samples.

Chondrules in the unaltered Kainsaz are clearly defined and composed primarily of forsterite, enstatite and augite, while plagioclase is present as an accessory mineral. Rounded Fe-Ni-metal and Fe-sulphide (troilite [FeS]) beads are also common components of chondrules. Chondrule mesostases are composed of mixed plagioclase and nepheline with minor Ca-feldspar, often appearing as lamellae intergrowths. Pristine chondrule glass is rare and found only as isolated regions in the cores of chondrules. The lack of chondrule glass is due to low-grade parent body metasomatic alteration (Tomeoka and Itoh, 2004; Bonato, 2020).

The fine-grained matrix in the unaltered Kainsaz has a dark (low Z value in BSE images), porous and "fluffy" appearance (Fig. 1A). Most mineral grains are submicrometre in size (ranging from 200 nm to 1.3 μm [Bonato, 2020]) and therefore difficult to discern, even in high-magnification SEM images. Larger (>3μm), irregular-shaped grains are however common, and are primarily Fe-rich olivine (fayalite) with occasional Fe-Ni-metal and rare Fe-sulphides. The average Fa composition of the unaltered Kainsaz matrix, is Fa47.8 (±6.9 [1σ], Table S1, Fig. 2).

We calculated modal mineralogy for the unaltered Kainsaz using the PSD-XRD technique (Table S2). This revealed an assemblage composed of olivine (49.0 vol%), pyroxene (37.3 vol%), Fe-Ni-metal (5.8 vol%), Ca-rich feldspar and nepheline (3.5 vol%), Fe-sulphides (4.2 vol%) and magnetite (0.3 vol%). These values are similar to those previously reported by Bonato (2020).

TGA revealed that the unaltered Kainsaz contains minimal volatiles. A powdered sample heated in the standard N_2 atmosphere increased in mass gradually as temperatures

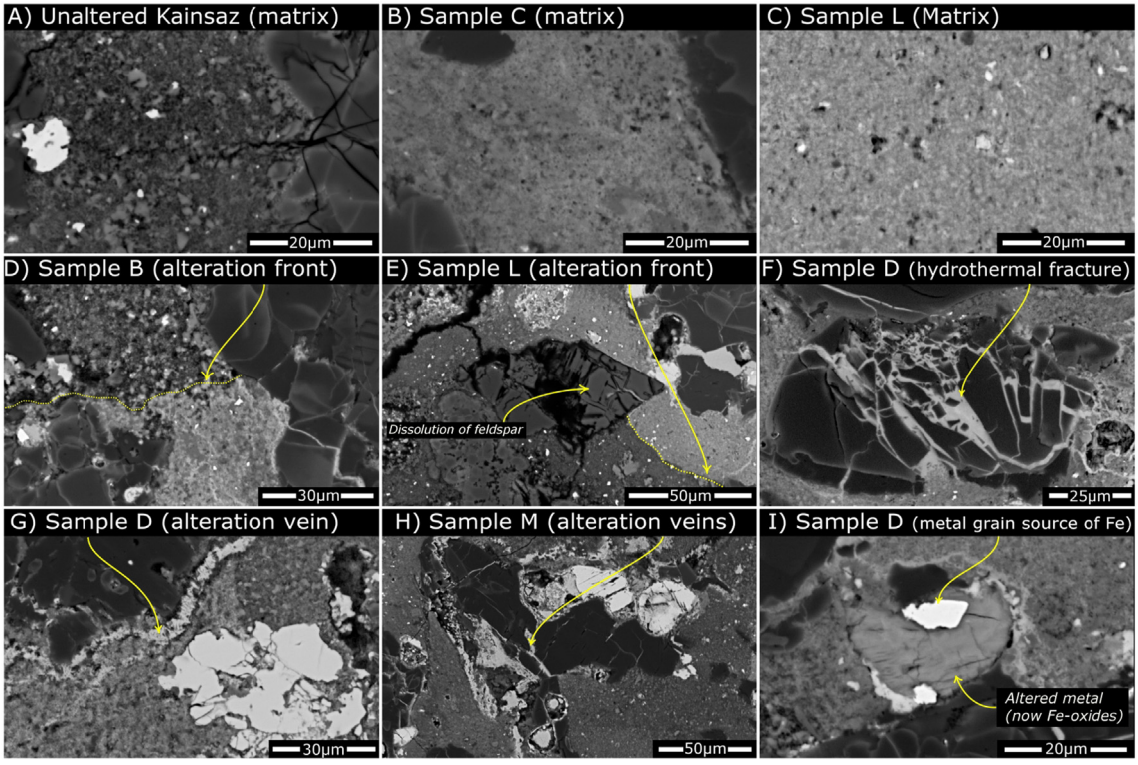

Fig. 1. SEM-BSE images of the fine-grained matrix in unaltered Kainsaz (panel A) and the altered samples (panels B-I). Panels B and C show the typical appearance of highly altered matrix illustrating the homogenous "fused" texture and brighter Z-values characteristic of Fe-enrichment. Panels D and E show the presence of alteration fronts where less-altered matrix is in direct contact with highly altered matrix and a sharp compositional boundary can be seen. Panel F shows the presence of highly fractured anhydrous silicate grain, with the fractures infilled by Fe-oxyhydroxide phases – evidence of hydrothermal fracturing processes during alteration. Panels G and H show the presence of Fe-rich veins composed of Fe-oxyhydroxides cutting across the matrix and through sulphide/silicate grains. Panel I shows a highly altered former metal grain that retains a small amount of residual unaltered metal. These grains would have acted as a source of Fe during alteration.

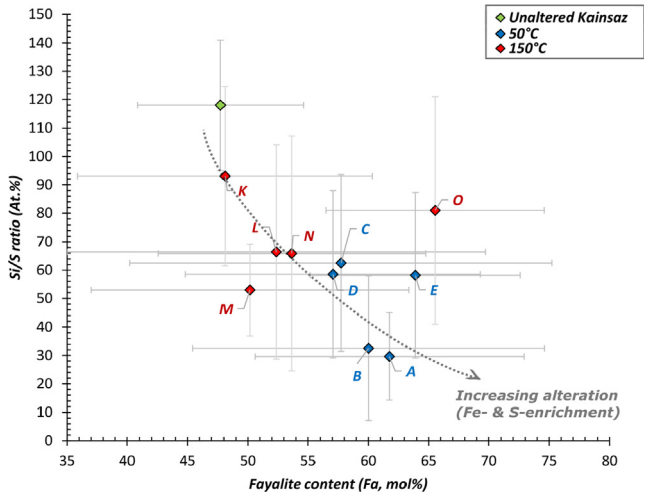

Fig. 2. Chemical composition of fine-grained matrix in the studied materials. This plot compares data from the unaltered Kainsaz (shown in green) against the altered samples (shown in blue [50 °C] and red [150 °C]). In all instances alteration resulted in significant enrichment in both Fe and S. This effect is most extreme in the low-temperature samples. This geochemical trend most likely reflects the formation of new fayalite, Fe-oxyhydroxides and Fe-sulphides grains which precipitated from solution during alteration. Error bars mark 1σ standard deviation.

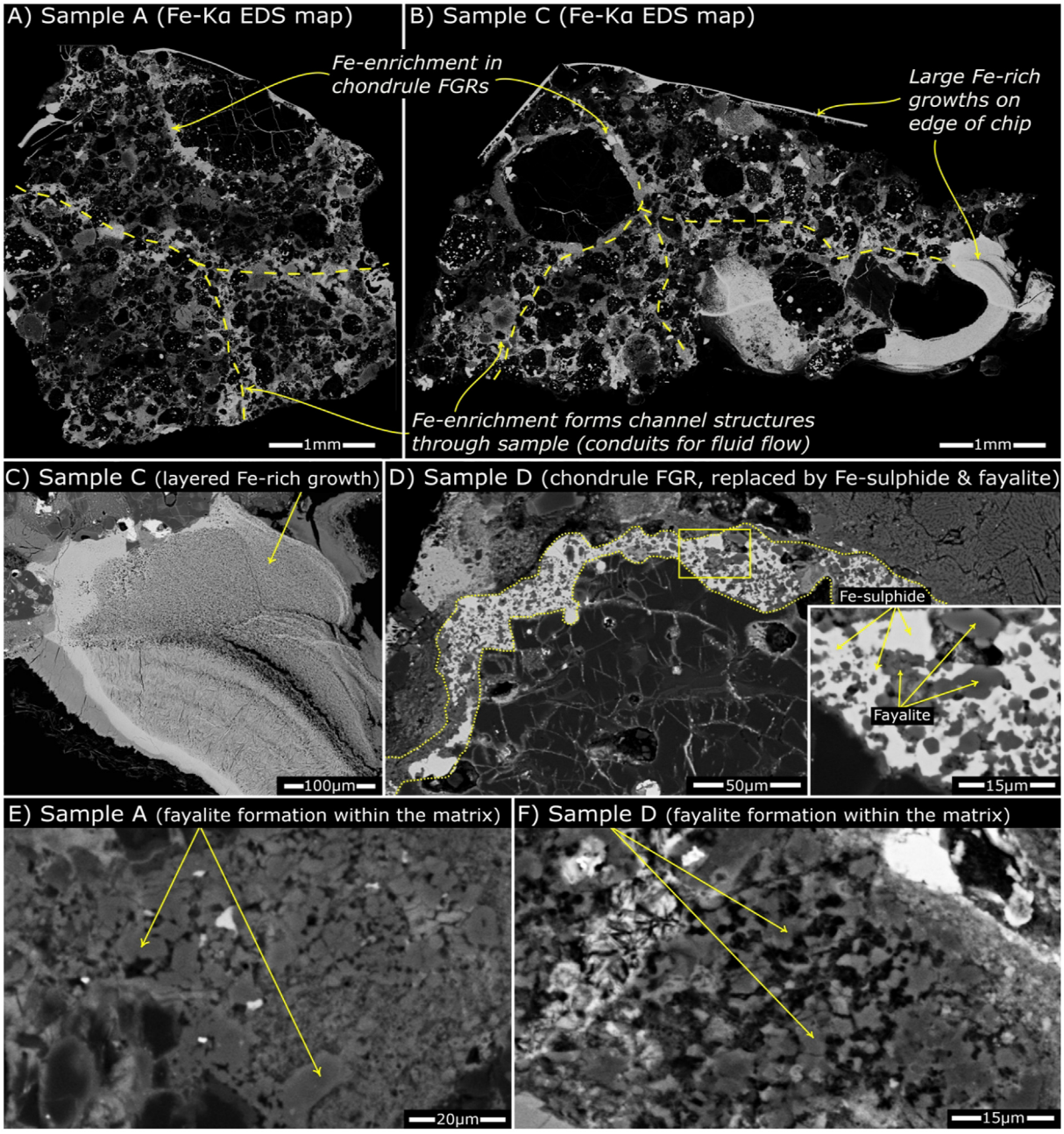

Fig. 3. Hydrothermal alteration resulted in significant Fe mobilization and redeposition. This can be observed in single element Fe-Kα maps (panels A and B) and reveals the presence of Fe-enriched channels that have formed within the fine-grained matrix and along chondrule FGRs. Also present are large Fe-rich growths at the edge of the specimen in sample A (panel A), sample C (panel B) and sample D (not shown). Panel C shows a magnified version of the Fe-rich growth, revealing its layered structure and differing textures. Panel D shows the formation of large fayalite grains embedded in a mass of Fe-sulphides in sample D. These textures are not seen in the unaltered Kainsaz and therefore formed during alteration. Likewise, Panels E and F show large, rounded fayalite grains within the fine-grained matrix, their size, location and homogenous composition (reflected in their homogenous Z-value) are distinct from the fayalite grains observed in the matrix of the unaltered Kainsaz. The presence of Fe-enrichment allows the movement of fluids to be traced and suggest the extent of alteration was strongly controlled by permeability and the local availability of water.

rose above ~ 350 °C, ending with a total change of +0.3 wt% (Table S3). This mass increase most likely reflects minor oxidation of Fe-metal due to the trace impurities (including O_2 at ~ 5 ppm, moisture at ~ 5 ppm and carbon dioxide at ~ 2 ppm) that are present in the N_2 atmosphere.

4.3. Mineral chemistry and alteration textures observed under SEM

The alteration style, secondary minerals and their petrographic textures are similar among all the altered samples,

and description of their textures and phase relations are therefore treated together.

4.3.1. Fine-grained matrix

Localised regions of fine-grained matrix in all the altered samples have clear evidence of modification by fluids. They show distinct Fe-enrichment, with increases in their average Fa content from Fa47.8 up to Fa63.9, as well as modest increases in S content (Fig. 2, Fig. S3), with at.% Si/S ratios dropping from ~ 120 in the unaltered Kainsaz to values between 30 to 95. Similar trends of enrichment are observed for Ni (Table S1). Correspondingly, decreases in Mg, Si, Cr and Mn are also observed (relative to the unaltered Kainsaz composition). These trends demonstrate that the principal elements that have experienced redistribution during hydrothermal alteration are Fe, Ni and S.

In addition to chemical alteration, the texture of these altered matrix zones are characterised by a brighter appearance (higher Z values) in BSE images and a "fused" homogenous texture (Fig. 1B and C). These altered regions appear to be less porous and retain fewer grains with clear grain boundaries. In many instances dark, apparently unaltered or only mildly altered regions of matrix were found in direct contact with regions of heavily altered matrix (as shown in Fig. 1D and E). At larger length scales and in the more extensively altered samples (e.g. A, C and D), single element Fe EDS maps (Fig. 3A and B) reveal how these localised regions of highly altered matrix are distributed throughout the sample. They formed wide (>100 μm thick) elongated channels with branching profiles. Notably these channels cut through the matrix and chondrule fine-grained rims (FGRs) (Fig. 3A and B).

4.3.2. Fe-rich phases, veins and overgrowth structures

Abundant Fe-rich phases formed during hydrothermal alteration; they were observed under SEM in all the altered samples as small Fe-rich alteration veins (Fig. 1F, G and H). These Fe-rich veins are numerous within the fine-grained matrix and generally appear as thin (≪10 μm wide) and porous structures with sinuous, branching profiles. Veins were also seen to crosscut through chondrules and penetrate anhydrous silicates along fractures. In several instances we observed large anhydrous silicate grains affected by extensive fracturing and where the fractured void space had been infilled by Fe-rich veins (Fig. 1F). In addition to these small-scale features, larger Fe-rich masses with complex growth structures adhering to the edge of the meteorite chip or infilling internal void spaces were observed in three of the low-temperature experiments (samples A, C and D [Fig. 3A–C]). They display a range of textures from compact and homogenous to fibrous (appearing as dense clusters of aligned needles) or porous forms with a speckled texture. These large growths are commonly layered with variable textures. Spot EDS analyses on both the Fe-rich veins and the larger Fe-rich growths reveal compositions dominated by Fe and O. Although direct quantification of O by EDX does not carry a high degree of accuracy, analysis of atomic O/(Fe + Ni) ratios provides an indication of the phases present. The O/(Fe + Ni) ratios vary from values around 1:1 to 2.5:1 and most likely reflect a range of closely related Fe-oxyhydroxides and Fe-oxide phases (e.g. goethite and magnetite as well as potentially lepidocrocite, ferrihydrite and hematite). Small quantities of Si are also detected (generally < 3 wt% and in all instances < 8 wt%) in some analyses from each sample (Fig. 4), indicating the possibility of minor contributions from fine-grained Fe-rich phyllosilicates intermixed with the Fe-oxyhydroxides and Fe-oxides. Note that, thermody-

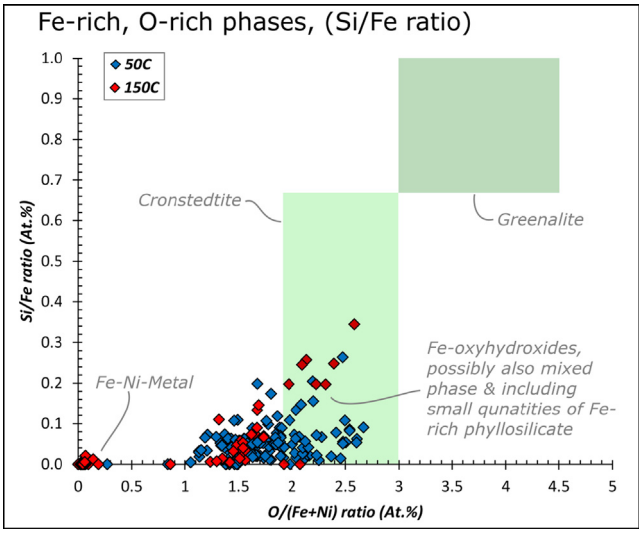

Fig. 4. Chemical compositions of the Fe-rich, O-rich phases in the altered samples. Fe-Ni metal acted as a source of Fe. These alteration phases have variable compositions with atomic O/(Fe + Ni) ratios varying from 2.5:1 to 1:1. They likely correspond to a range of Fe-oxyhydroxides/oxides including goethite (2:1) and magnetite (1.3:1). Some of these phases contain small quantities of Si. Also shown are the compositional ranges of Fe-rich phyllosilicates (cronstedtite and greenalite). Elevated Si abundances could indicate the presence of minor phyllosilicate intermixed with the Fe-oxyhydroxides.

namic calculations show the stability field for cronstedtite decreases with increasing temperature, becoming negligible at ~150 °C. Consequently the inferred phyllosilicate minerals are most likely greenalite (Pignatelli et al. 2014; Vacher et al. 2019b). This inference was supported by geochemical modelling, which indicated that greenalite would be thermodynamically stable within these environments.

4.3.3. Chondrules and mesostasis

In the experimentally altered samples anhydrous Fe-Mg chondrule silicates were unaltered, with no textural evidence of chemical attack. Furthermore, the chondrule mesostases were similar in appearance and mineralogy to the unaltered Kainsaz. They were composed of intermixed nepheline and Ca-rich plagioclase with a lamellae texture composed of extremely fine-grained (<1μm) intergrowths. Furthermore, in some instances the texture of chondrule mesostases had coarsened and no longer appeared as lamellae but instead had a cellular habit, composed of intermixed alkali-rich phases (feldspar, nepheline and Ca-rich pyroxene) with grain sizes on the order of 1–3 μm (Fig. 5A).

4.3.4. Fe-sulphide and fayalite

There is evidence for both Fe-sulphide and fayalite formation in the altered samples. As previously noted, the S abundance in the fine-grained matrix is consistently higher in the altered samples (relative to the unaltered Kainsaz matrix), implying the presence of newly formed submicrometre Fe-sulphides. In addition, analysis of larger (5–50 μm-sized) Fe-sulphide grains (Fig. 6) revealed subtle chemical differences between those found in the altered samples and those found in the unaltered Kainsaz. The (Fe + Ni)/S ratio of sulphides in the high temperature altered samples are, on average, lower than the values observed in the unaltered Kainsaz (unaltered: 0.98 ± 0.02 [1σ], 50 °C: 0.98 ± 0.04 [1σ] and 150 °C: 0.92 ± 0.06 [1σ]). Finally, we identified a new population of high-Ni (Ni > 10 at.%) pyrrhotites (Fig. 6) found only in the high-temperature samples. Their distinct compositions are clear evidence of new sulphide formation.

At larger scales, rare instances of mixed sulphide and fayalite masses are present. For example, in sample D (Fig. 3D) we found a thick (15–50 μm) growth rim running along the edge of a large chondrule. This rim is composed of small, rounded fayalite grains (~5–10 μm sized) with a uniform composition (Fa49) embedded in a groundmass of Fe-sulphides (troilite). These large masses of mixed Fe-sulphide and fayalite are not present in the unaltered Kainsaz but are present in several other experimental samples, being more common in the high-temperature experiments (namely K, L, M and O). High magnification images of the fine-grained matrix in the altered samples also revealed evidence of fayalite growth (without associated Fe-sulphide formation). In some regions of heavily altered matrix large individual fayalite grains reach sizes of 10–30 μm (Fig. 3E and F). They have a homogenous appearance in BSE images, Fe-rich compositions (>Fa55) with minimal minor element concentrations and subhedral morphologies which form a fused or merged texture where grain boundaries meet. Grains with these forms are absent from the unaltered Kainsaz lithology.

4.3.5. Carbonates

Carbonates are absent in the unaltered Kainsaz but were present in all the altered samples where they occurred as a minor phase. They were most commonly found located at the edge of the meteorite chip (Fig. 5D) or, less commonly seen to have infilled rounded voids within chondrule cores ([Fig. 5E and F] most likely infilling voids left after the dissolution of Fe-Ni-metal). Carbonates therefore demonstrated a preference to precipitate into void space. In sample L we observed an interrupted episode of calcite formation (Fig. 5E). BSE images show numerous small lath-shaped calcite grains growing within a void inside a chondrule. These laths have a profusion of acicular growths extending from their margins, resulting in a fibrous network of calcite crystals with a cross-stitch texture. The most unusual carbonate grain observed was that identified in sample A. This grain (Fig. 5F) has an anhedral form due to the irregular shape of the void it has infilled. In addition, a thin rim of Fe-sulphides decorates the carbonate's margin. The morphology and phase relationships of this carbonate grain are therefore similar to the T1b calcites found in CM chondrites, which are decorated by grains of Fe-Ni metal or Fe-sulphides along their perimeter (e.g. Vacher et al. 2017). In all cases the carbonates found in the altered samples were calcites, based on their stoichiometric compositions (and later confirmed by IR reflectance spectroscopy). They contained minor quantities of Fe (0.2–1.6 wt%, avg: 0.5 wt%) and trace quantities of Na (0.0–0.5 wt%, avg: 0.2 wt%) and Mg (0.0–0.7 wt%, avg: 0.2 wt%).

4.3.6. Other accessory minerals

Other minor phases found in the altered samples include Fe-sulphate and gypsum. Fe-sulphate is rare (identified only in Samples A and D). The largest mass of sulphate (found in sample D, Fig. 5B) appears as a ~ 70 μm diameter irregular-shaped growth with a fibrous texture. It is embedded in a region of heavily altered matrix and co-occurs with extensive Fe-oxyhydroxide masses. Gypsum was identified in only a single sample (O) where it occurs as a thin vein that extends through the fine-grained matrix and infills a fracture within an olivine grain (Fig. 5C). This gypsum vein has embedded low-Ca pyroxene grains with relatively Mg-rich compositions (En61, Wo8), that may be either silicate formed during alteration or silicates that were present prior to alteration.

4.4. Bulk mineralogy identified from XRD

In every case the modal mineralogy of the altered samples was similar to the unaltered Kainsaz (Table S2). The dominant minerals remained olivine (>40 vol%) and pyroxene (>35 vol%), with minor quantities of feldspar (1.3–4.4 vol%) and detectable but often negligible quantities of nepheline (<2.2 vol%). The most obvious effect of alteration was a reduction in the abundance of Fe-Ni-metal (on average a loss of 3.2 vol%) and the subsequent formation of goethite, with goethite peaks observed in XRD

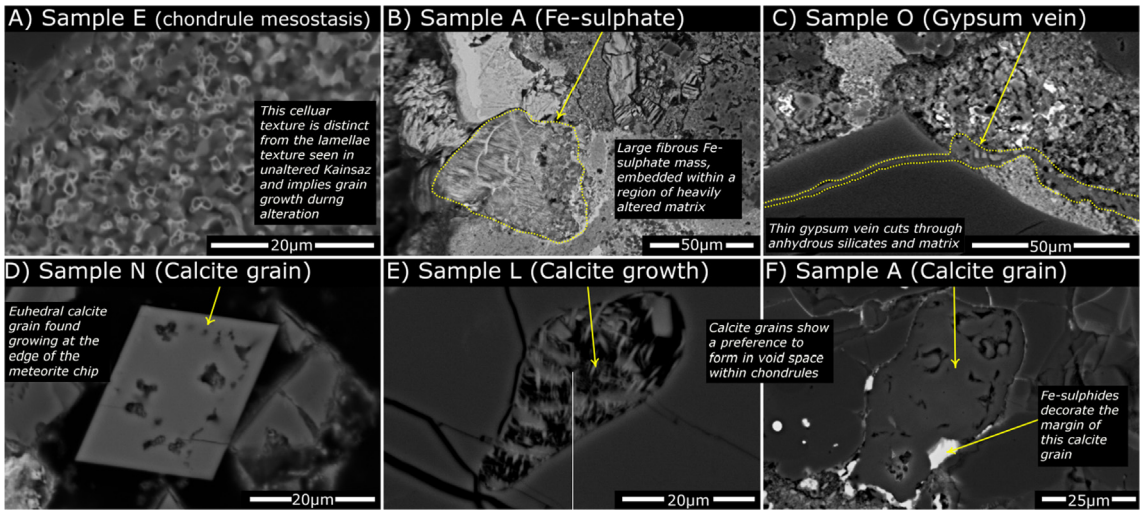

Fig. 5. Accessory minerals identified in the altered samples. Including: (A) Altered chondrule mesostasis, showing a cellular texture, as distinct from the lamellae textures observed in the unaltered Kainsaz. (B) A large mass of Fe-sulphate embedded within a region of heavily altered matrix. (C) A micrometre-sized gypsum vein that cuts through a fractured primary olivine grain. (D-F) examples of calcite growth, as euhedral forms occurring at the margin of the meteorite chip (D), and as irregular-shaped forms infilling voids left inside chondrules (E & F). Note that the calcite grain shown in F has a margin of Fe-sulphides.

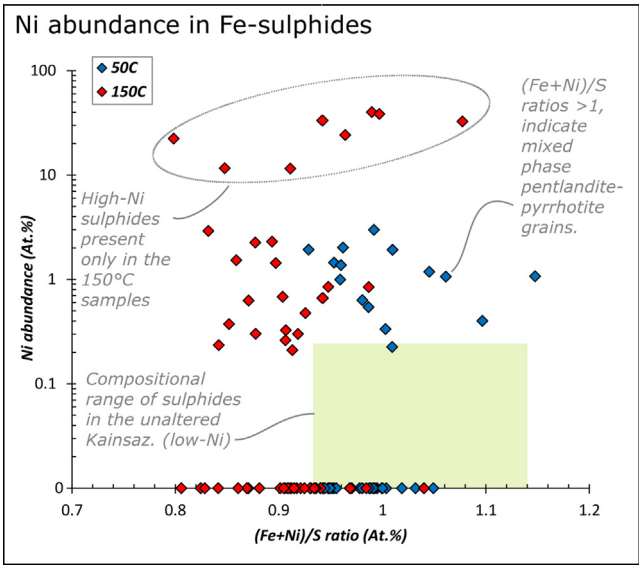

Fig. 6. Analyses of Fe-sulphides. Low-Ni sulphides are common in all samples, while high-Ni sulphides formed only in the high-temperature samples. Sulphides in the unaltered Kainsaz and low-temperature altered samples have average (Fe + Ni)/S ratios around 0.98, while the high-temperature altered samples have (Fe + Ni)/S ratios averaging 0.92. Note that (Fe + Ni)/S ratios >1 indicate the presence of pentlandite exsolution lamellae within a host pyrrhotite grain.

patterns and inferred abundances varying between 1.3 vol% and 9.9 vol%. Magnetite was another common mineral found in the altered samples at abundances between 0.6–3.3 vol% and that otherwise occurred in a very low abundance (0.3 vol%) in the unaltered Kainsaz. Trace quantities of Fe-sulphate (gypsum) were detectable in most of the altered samples but at concentrations too low to quantify. Diffraction features relating to phyllosilicates and/or carbonates were not detected in any of the altered samples. Analysis of the XRD pattern residual backgrounds allowed an estimation for the upper limit on the potential amount of poorly crystalline Fe-rich phyllosilicate that could theoretically be present in the altered samples. We arrived at values < 2 vol%. Our QPA results for each sample are given in Table S2.

4.5. Volatile content measured by TGA

All of the altered samples (A-E and K-Q) lost mass during TGA heating (Fig. 7). In general, the low-temperature samples lost more mass (average: −5.2%) than the high-temperature samples (average: −4.2%), indicating that they

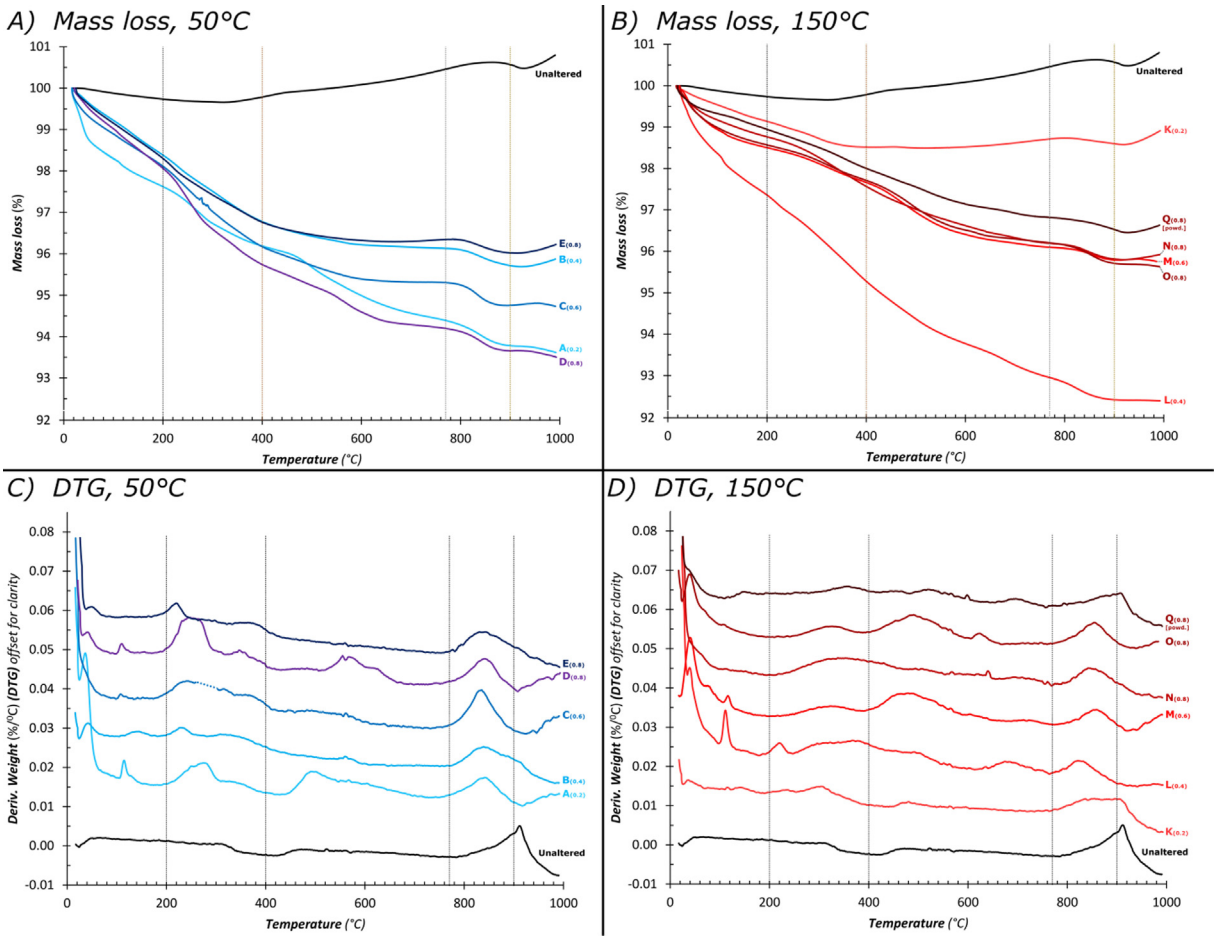

Fig. 7. Thermogravimetric data illustrating temperature-dependent mass loss due to the release of volatile gases from the altered samples upon heating from room temperature (~20 °C) to 1000 °C. Volatile gasses are emitted as mineral phases thermally decompose. Low-temperature (50 °C) analyses (panels A and C) are shown in blue, while high-temperature (150 °C) samples (panels B and D) are shown in red. Panels A and B display mass loss as a function of temperature, while panels C and D display the differential thermogravimetry curves for each sample. The response of the unaltered Kainsaz is shown in black for reference. Peaks in the DTG curves indicate the thermal decomposition of specific mineral phases. Vertical dashed lines, located at 200 °C, 400 °C, 770 °C and 900 °C correspond to the ranges and boundaries conventionally attributed to the decomposition of volatiles from adsorbed water, Fe-oxyhydroxides, phyllosilicates, and carbonates respectively (as detailed in Garenne et al., 2014).

experienced more advanced alteration. However, there was also considerable variation within the two temperature batches.

On TGA plots the derivative of mass loss (panels C and D of Fig. 7) allows discrete volatile decomposition events to be identified. Conventionally the TGA plot of hydrated carbonaceous chondrites is split into four generalized regions (shown in Fig. 7) corresponding to the loss of volatiles from adsorbed water (0–200 °C), Fe-oxyhydroxides (200–400 °C), phyllosilicates (400–770 °C) and carbonates (770–900 °C) (e.g. Garenne et al., 2014; King et al. 2015). However, this simplified approach overlooks any contribution of volatile gas release from S-bearing minerals (sulphides and sulphates) and organics which may be present in non-negligible quantities.

Some decomposition peaks can be assigned to the loss of volatile-bearing phases using existing knowledge of sample mineralogy (as inferred from XRD/SEM) and by comparison against data from mineral standards. The lowest temperature peak (~50 °C) appearing in most of the altered samples as a small, rounded bump most likely corresponds to the thermal decomposition of ferrihydrite (previously detected in the XRD data) and which decomposes at T < 100 °C. At slightly higher temperatures, several samples have a small, sharp peak located at ~ 120 °C. This peak is characteristic of gypsum (Janssens, 2011). At higher temperatures, peaks between 200–400 °C, which are generally narrower and more prominent in the low-temperature samples are associated with Fe-oxyhydroxides. In the altered samples the main peaks within this range are centred between 225 °C and 310 °C, corresponding to goethite decomposition. Decomposition peaks in the 200–400 °C region may also correspond to the release of S_2 gas from minerals in the pyrrhotite-troilite solid solution ($Fe_{(1-x)}S$ [x = 0 to 0.2]). Sulphides, which are common in the altered samples are therefore likely also contributing to the observed mass loss over this region.

DTG peaks over the temperature range 400–770 °C range are commonly attributed to water release from phyllosilicates

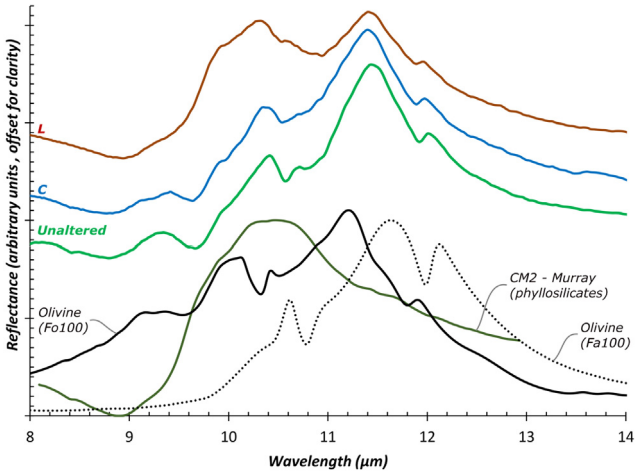

Fig. 8. Average mid-IR reflectance spectra (8–14 μm silicate fingerprint region) of the fine-grained matrix in the 50 °C samples (shown in blue and represented by sample C) and the 150 °C samples (shown in red and represented by sample L). The unaltered Kainsaz is also shown (in green). Spectra of olivine (both the Mg-end member [Fo100] and the Fe-end member [Fa100] are included) and the matrix of CM2 chondrite Murray are given (in black) for reference. The matrix in the unaltered Kainsaz is dominated by fayalitic olivine. Spectra of the low-temperature samples are consistent with an olivine composition. The high-temperature samples (all except sample K) have spectra resembling a mixture of olivine and phyllosilicates. Note: matrix spectra from each sample are given in Fig. S4.

(e.g. Garenne et al. 2014). For the low-temperature samples mass loss over this range was generally minimal, with samples B, C and E having flat profiles. Meanwhile, samples A and D, as well as the high-temperature samples (except sample K) have shallow negative sloped mass loss profiles. This could correspond to water released from phyllosilicates or sulphur released from sulphides or SO_2 gas released from Fe-sulphates (which decompose at temperatures between 500 °C-600 °C [Siriwardane et al. 1999]). With the current data is it not possible to discern what phases these peaks relate to. However, if we assume that the entire mass loss over the 400 °C-770 °C window was due to the loss of water (OH–molecules) we can estimate an upper limit on the potential amount of phyllosilicate. Our cronstedtite mineral standard (BM52294) loses ~ 10 wt% when heated on the TGA instrument. On average the altered samples lost ~ 1.1 wt% over the 400 °C-770 °C range, this would correspond to total phyllosilicate abundances in the altered samples of < 11 wt%.

Finally, all the altered samples (with the exception of sample Q) have a distinctive mass loss event in the 770–900 °C temperature range (which is otherwise absent from the unaltered Kainsaz). DTG curves show the peak centre lies between 830 °C and 875 °C. This feature may correspond to the decomposition of calcite and the release of CO_2 gas, since calcite was positively identified under SEM. However, decomposition temperatures >800 °C are atypical for calcite, with tends to rapidly decomposes around 750 °C (Karunadasa et al. 2019).

4.6. Matrix mineralogy inferred from IR spectroscopy

The averaged (3 < n < 10) mid-IR spectrum of the fine-grained matrix in the altered samples presented either with an olivine signature or a combined olivine and phyllosilicate signature (Fig. 8 and S4). All the low-temperature 50 °C samples and sample K showed only an olivine feature. This is the same as the unaltered Kainsaz spectral signature and suggests that the fine-grained matrix was dominated by crystalline olivine (with an Fe-rich, fayalitic composition). By contrast, the IR spectra of the high-temperature (150 °C) samples also contained a broad, smooth peak located at approximately 10.3 μm and with a shoulder peak at ~ 9.9 μm. This shape is very similar to the spectral profile of the CM chondrites (as demonstrated by the comparison with the matrix of CM2 Murray) and therefore strongly suggests the presence of hydrated phyllosilicates. The data from samples L, M, N and O is best explained if their matrices are dominated by olivine but contain minor contributions of phyllosilicate (<2 vol % based on the XRD data).

4.7. Bulk O-isotope data

The isotopically doped ^{17}O-rich heavy water used in this study has a composition of $\delta^{17}O$: +64.5‰, $\delta^{18}O$: −3.9‰ and $\Delta^{17}O$: +66.5‰ [Table 2]). Five samples (D, E, N, O and Q) were reacted with heavy water. The bulk O-isotope compositions of these five altered samples (Fig. 9A) increased in $\Delta^{17}O$ relative to the unaltered Kainsaz composition, with increases between + 5.9‰ and + 16.3‰. By contrast, changes in $\delta^{18}O$ relative to the unaltered Kainsaz are less extreme and ranged from a decrease of −1.9‰ in sample E to increases in the remaining four samples (D, N, O and Q) by up to + 2.7‰.

5. DISCUSSION

5.1. Insights from geochemical models

Thermochemical modelling predicted similar secondary mineral assemblages for both temperature conditions (Fig. 10). At 50 °C the alteration of the chondrule-free material resulted in secondary mineral assemblages that

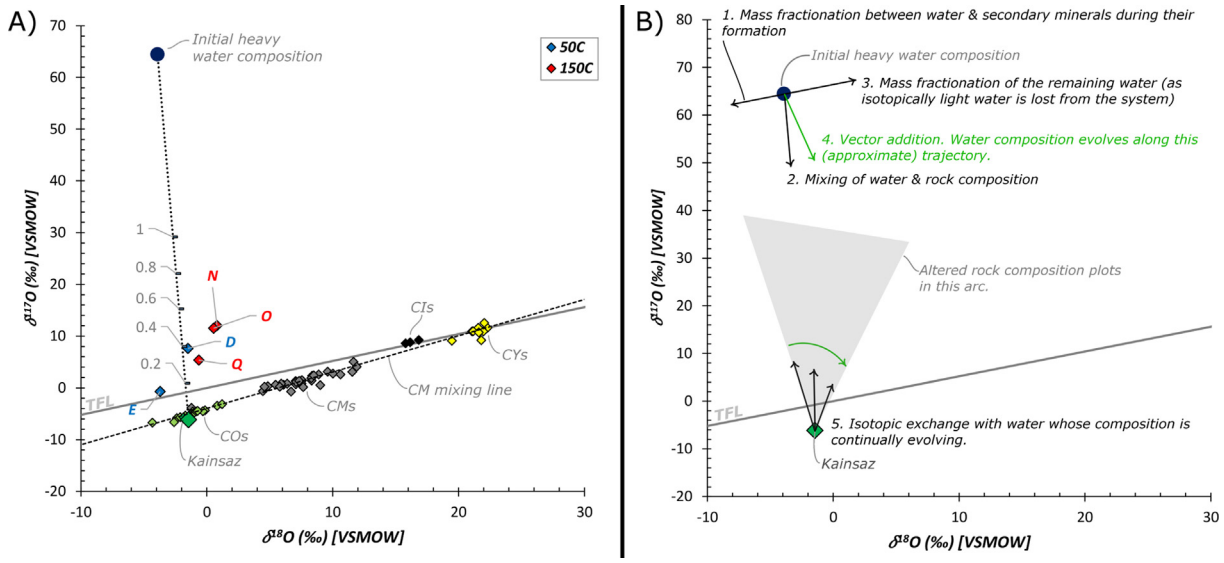

Fig. 9. (A) Bulk O-isotope data for the five samples (D, E, N, O & Q) altered with doped heavy water. They are compared against the composition of unaltered Kainsaz (large green diamond), and the composition of the doped heavy water (large purple circle). A dotted black tie-line links these two values. Theoretically, in an idealized closed system, after all water has reacted the bulk compositions of the altered samples should plot on this line. Tick marks denote the expected final composition for a given initial W/R_E ratio. All the altered samples have increased in $\Delta^{17}O$ relative to their starting composition (the unaltered Kainsaz, large green diamond). However, none of the altered samples plot on the tie-line. Instead, their positions are shifted, in most instances, having fractionated to heavier ^{18}O-enriched compositions. This is primarily due to open system behaviour resulting in the preferential loss of isotopically light water under a mass-dependent regime. Also shown for reference are the bulk compositions of the COs, CMs, CYs and CIs chondrites, the TFL and the CM mixing line. These data were taken from Clayton and Mayeda (1999), Moriarty et al. (2009), Alexander et al. (2018). (B) Supporting diagram explaining how the composition of the water and rock evolve as the experiment proceeds under the competing effects of mass fractionation between water and secondary minerals, mass fractionation during open system water loss and mixing between the evolving water composition and the rock composition. (For interpretation of the references to colour in this figure legend, the reader is referred to the web version of this article.)

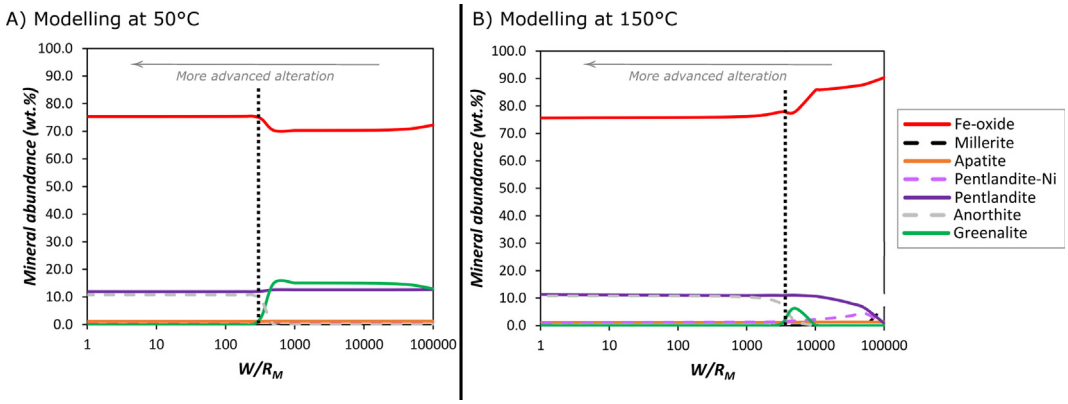

Fig. 10. Modelled secondary mineral assemblages formed in equilibrium at (A) 50 °C and (B) 150 °C. Vertical dashed lines indicate the inferred effective W/R, that is the amount of rock that is inferred to have reacted with fluids. These values are approximately 250 for the 50 °C experiments and 3300 for the 150 °C experiments.

were dominated (70–75 wt%) by Fe-oxides across all W/R_M. At high W/R_M (100,000) greenalite and pentlandite ($Fe_{4.5}Ni_{4.5}S_8$) were predicted in abundances between 12–15 wt%. As the reaction progressed to an intermediate W/R_M of 250 the Ni-rich endmember of pentlandite-Ni (Ni_9S_8) became stable and the abundance of greenalite declined to 0 wt%, which led to anorthite ($CaAl_2Si_2O_8$) precipitation as Si became available. The system remained stable as more host rock was reacted and resulted in a Fe-oxide-pentlandite-anorthite mineral assemblage between a W/R_M of 250 to 1. Minor quantities (<2wt.%) of hydroxyapatite and Ni-rich pentlandite are also expected to form. At a higher temperature of 150 °C secondary minerals were similar to those that formed at 50°C, however, a variation in mineral abundances was observed. Fe-oxides were abundant across all W/R_M ratios. At high W/R_M (100,000) 89 wt% Fe-oxide was predicted, however, this declined as the reaction progressed to 75–76 wt% with additional

Fe-bearing minerals instead forming. At high W/R_M millerite (NiS) was the dominant sulphide mineral precipitated, however, pentlandite ($Fe_{4.5}Ni_{4.5}S_8$) became more stable at a W/R_M of 52,000 and progressively became the most abundant sulphide. Greenalite precipitation occurred over only a very narrow W/R_M around 5000, unlike models at 50 °C that saw greenalite form across a broader W/R_M. Anorthite began to precipitate from a W/R_M of 10,000 and developed into one of the dominant secondary minerals from a W/R_M 3300 when greenalite became unstable. The system stabilised forming a Fe-oxide-pentlandite-anorthite secondary mineral assemblage at a W/R_M of 1400, which was higher than what was observed for models at 50 °C (W/R_M of 250).

The results of our geochemical modelling (Fig. 10) compare favourably with the observed secondary mineral assemblages generated in our experiments (Sections 3.3–3.6). At both temperature regimes the models predicted alteration assemblages dominated by Fe-oxides coexisting with minor quantities of Fe-sulphides and plagioclase (anorthite) as well as trace amounts of Fe-rich phyllosilicate (greenalite) and Ca-phosphate (apatite). Abundant Fe-oxides and oxyhydroxides were formed in our experiments, in agreement with the model. Likewise, a range of Fe-sulphides were formed. Although we did not observe secondary anorthite, this phase was expected only in the advanced stages of alteration. Its absence therefore suggests alteration did not progress this far. Furthermore, the absence of anorthite can be used to estimate the relative extent of alteration at the two different temperatures. Modelled W/R_M gave values of ≤ 250 and ~ 3300 for the 50 °C and 150 °C systems. This indicates that the low temperature reactions progressed further than those conducted at 150 °C. This conclusion is consistent with our independent estimate of alteration extent discussed below in Section 5.7.

5.2. Open system behaviour

We conclude that partial open system behaviour affected all experiments in this study. Two independent lines of evidence support this interpretation.

(i) Mass balance calculations comparing the starting mass (initial rock plus the added water) are consistently higher than the final measured masses (with deficits of between 10% and 40% for the final masses). At the end of experiments either minimal water or no water remained. This requires that a non-negligible fraction of the initial water escaped the reaction vessels during the experiments. The values shown in Table 1 indicate the inferred amount of water that remained unreacted (primarily due to loss from the reaction vessels).

(ii) The measured bulk O-isotope compositions of the altered samples where no water remained at the end of the experiments (samples N, O and Q) should plot on a mixing line between the two starting components (Fig. 9A). However, the compositions of these samples do not plot on the mixing line but are instead offset to more $\delta^{18}O$-enriched compositions. These fractionation effects are consistent with an open system environment (as discussed in detail in Section 5.9).

5.3. The conversion of Fe-metal to Fe-oxyhydroxides: Fe transport, fluid flow and pH conditions

The modal mineralogy revealed extensive kamacite corrosion, with metal nearly completely absent in samples A and D (Table S2). Supporting evidence that kamacite grains were the main source of Fe is shown in Fig. 1I. Pourbaix diagrams (Eh/pH plots [Fig. 11A and B]) show that Fe-metal is unstable when in contact with water and will therefore either corrode (dissolving into solution under acidic conditions) or passivate (forming hydroxyl-bearing minerals under alkaline conditions). Our experiments produced extensive goethite and magnetite deposits. While goethite has a relatively wide range of precipitation conditions, magnetite's formation window is more restrictive. At 50 °C (Fig. 11A), magnetite forms at pH conditions >6 and Eh values < 0. At higher temperatures (150 °C, Fig. 11B) magnetite's stability field is slightly enlarged. This region can be used to estimate early fluid conditions (implying a range from slightly acidic [pH: 6] to strongly alkaline [pH: 14]).

Oxidation reactions that facilitated kamacite dissolution would have consumed large quantities of H^+ ions, as shown by the two half-cell reactions:

$$Fe^0 \rightarrow Fe^{2+} + 2e^- \quad (3)$$

and

$$2H^+ + 2e^- \rightarrow H_2 \quad (4)$$

Furthermore, additional H^+ ions would have been consumed to make further H_2(g) during the conversion of ferrous Fe to ferric Fe.

$$Fe^{2+} \rightarrow Fe^{3+} + e^- \quad (5)$$

The resulting loss of H^+ ions would push fluid compositions towards increasingly alkaline conditions, whilst also generating H_2 gas, which would have slowly escaped the reaction vessels due to open system loss (Section 4.2) thereby maintaining an oxidizing environment through the effective removal of reducing gases (Guo and Eiler, 2007; Le Guillou et al. 2015). Although alkaline conditions promote the precipitation of Fe-oxides and Fe-oxyhydroxides, these same conditions also mean that dissolved Fe ions have short lifetimes in solution and are unlikely to be transported far from their site of dissolution before being precipitated (Pourbaix and DeZoubov, 1974; Beverskog and Puigdomenech, 1996). At the fine-scale, evidence for the rapid precipitation of Fe-oxides and Fe-oxyhydroxides is observed. Regions of heavily altered matrix abut against less-altered matrix (Fig. 1D) forming the appearance of alteration fronts. Because the main chemical changes are the addition of Fe and S (Fig. 2), we can conclude that these reactions were primarily precipitation (as opposed to leaching), leading to the depletion of $Fe^{2+/3+}$ and S^{2-} ions from the fluid phase. The presence of alteration front textures implies that the unaltered matrix readily reacted with the fluid phase, depleting dissolved ions and limiting further reactivity.

New mineral formation had the effect of lowering matrix porosity by infilling pore space. Comparison of the EDS weight totals collected on the unaltered Kainsaz matrix

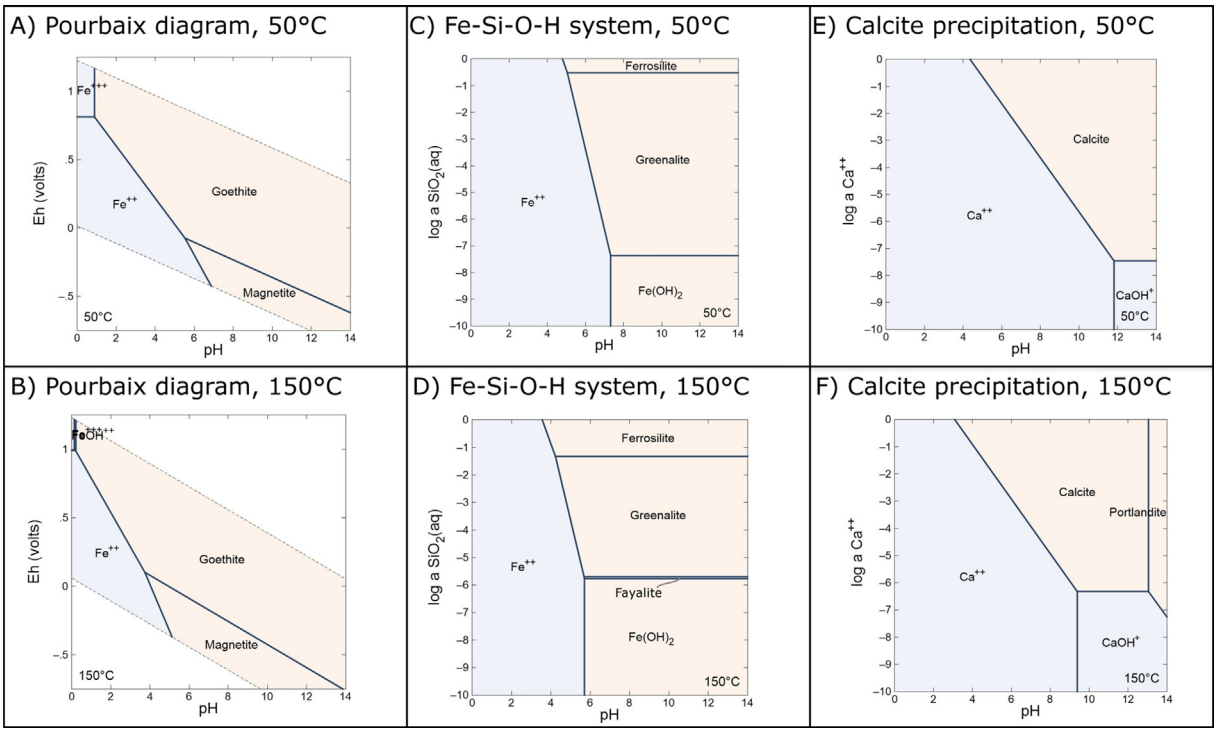

Fig. 11. Geochemical diagrams relevant to the alteration conditions in this study. A & B) Pourbaix diagrams for the Fe system, C & D) stability fields for minerals in the Fe-Si-O-H system as function of pH and silica activity ($aSiO_2$) and D & E) conditions for calcite precipitation. Plots A, C and E are for the low-temperature samples (50 °C, 1.15 bar), while plots B, D and F are for the high-temperature samples (150 °C, 4.78 bar). Plots A-D are for an Fe activity of $1e^{-03}$. All plots were generated using the Geochemist's workbench software. Note, aqueous phases are shown in blue while mineral precipitates are shown in beige.

(~81 wt%) and on the altered matrix (>90 wt%), as well as a visual comparison of different matrices (Fig. 1A vs. B and C), confirm that alteration reduced matrix porosity. Once depleted of Fe^{2+} and S^{2-} ions, circulating fluids would be less able to form new secondary phases and the system would instead favour further corrosion of metal. The widespread mobilization and redeposition of Fe (in the form of oxides and hydroxides) therefore requires a prolonged duration of alteration, in which the progressive consumption of kamacite added new Fe^{2+} ions into solution, replacing those depleted by precipitation. Over time the reactive alteration front (where Fe-bearing secondary mineralization occurred) were able to migrate further from the site of Fe dissolution, creating the observed alteration veins, fronts and, at the edge of the specimen (and only) in the most altered samples, the development of large Fe-rich growth structures.

The Fe-rich alteration features described above, as well as their fluid-rock interactions, have close similarities to features previously observed in CM chondrites. Hanowski and Brearley (2000) detailed the presence of large Fe-rich aureoles (with sizes on the order of 100′s micrometres to mm-scales) in several CM chondrites (Murchison, Murray and ALH 81002). These aureoles were composed of heavily altered fine-grained matrix and characterised by significant increases in FeO concentration (by up to 15 wt%) relative to the surrounding less-altered matrix. They had sharp compositional boundaries, a light brown colour under the optical microscope and formed mantles on tochilinite-cronstedtite masses or replaced the FGRs on chondrules. Similar features were more recently described by Haenecour et al. (2020) in the ungrouped CO-like chondrite MIL 07687. These phases, found in naturally altered chondrites are strikingly similar to the alteration features observed in our experiments. In both instances, their textures act as strong evidence of widespread Fe mobilization and redistribution, meanwhile the similarity between the two sets of samples suggest that the behaviour of fluids were similar in both environments.

5.4. The formation of phyllosilicates and fayalite

Abundant, high crystallinity phyllosilicate minerals were not formed in any experiment. Characterisation using SEM (Figs. 1 and 3) and XRD (Table S2) shows no direct indication of phyllosilicates. Although the TGA data (Fig. 7) suggests low abundances of phyllosilicates are possible, these data are inconclusive. By contrast, IR reflectance spectra (Fig. 8 and S4) collected on the fine-grained matrix revealed the presence of phyllosilicate minerals in some of the high-temperature samples (L, M, N and O). These results can be put into context by considering their analytical mechanism. Infrared spectroscopy detects molecular-scale vibrations, in this case Si-OH bonds in phyllosilicates. Conversely, SEM and XRD techniques are sensitive to larger grain-scale features. The lack of resolvable phyllosilicate diffraction peaks

in the XRD data and the absence of identifiable phyllosilicate grains under SEM suggest that any phyllosilicates occur either at low abundances (<2 vol%) and/or as nano-phase crystallites (<50 nm) with a low degree of crystallinity and a high degree of crystal-chemical disorder. They could be similar to the phyllosilicate-like gels reported by Changela and Bridges (2010) from the Martian nakhlites. The formation of phyllosilicates was therefore captured at an immature stage in our experiments.

Previous experimental research has demonstrated that the viability of Fe-rich phyllosilicate precipitation from aqueous solutions is dependent on the stability of a Fe $(OH)_2$ precursor phase, which forms the octahedral layers in Fe-bearing phyllosilicate minerals (Harder, 1978). Consequently, at low temperatures (approximately < 100 °C) Fe-bearing clays are predicted to form only under reducing conditions (Harder, 1978; Peng and Jing 2014). This is because reducing environments partially stabilize Fe $(OH)_2$, slowing its otherwise rapid (minutes to days) oxidative decomposition into magnetite, H_2 gas and water in a process known as the Schikorr reaction (Schikorr, 1929; Shipko and Douglas, 1956). Additional factors that promote the stability of $Fe(OH)_2$ in solution are dissolved silica, high pH alkaline environments (Shipko and Douglas, 1956; Peng and Jing 2014) and the presence of mackinawite-like ($Fe_{1-x}S$) layers in solution (Kakos et al. 1994; Peng et al. 2009). Some of these factors were present in our experiments. Conversely, under oxidizing conditions $Fe(OH)_2$ instead precipitates as a mix of goethite and amorphous Fe-hydroxides (Harder, 1978). Our experiments began with a small quantity (<2ml) of initial O_2 in the headspace of the reaction vessels which would have promoted oxidizing conditions. Furthermore, oxidizing conditions were predicted from the geochemical models (Section 5.1.) and confirmed by the oxidation of metal (Section 5.3.) and other minerals (e.g. sulphides). These conditions partially inhibited the ability of the hydrothermal system to form Fe-rich phyllosilicates from $Fe(OH)_2$ precursors. However, other experimental hydrothermal alteration studies have successfully produced phyllosilicates, including Fe-serpentines from natural samples (GEMS-bearing interplanetary dust particles) when exposed to water in reaction vessels which included atmospheric air as their headspace gas (thereby supplying initially oxidizing conditions) (Nakamura-Messenger et al. 2011). Thus, other factors probably also acted to inhibit phyllosilicate development. The other main factor that could prevent phyllosilicate formation is the crystallinity of the matrix and its effect on dissolved silica activities. Silica activity imparts a significant control on alteration style, principally by controlling the main secondary silicate minerals that can form (Brearley, 1995; Jones and Brearley, 2006; Zolotov et al., 2006; Ganino and Libourel, 2017). For example, on the CV parent body low silica activities appear to have produced andradite-bearing assemblages while higher silica activities produced kirschsteinite-bearing assemblages (Ganino and Libourel, 2017).

Our geochemical plots of the Fe-Si-O-H aqueous system (Fig. 11C and D) show that a range of minerals form under alkaline conditions dependent on silica activity. At low silica activities Fe-oxyhydroxides and Fe-oxides are stable (poorly crystalline $Fe[OH]_2$ is predicted in Fig. 11C and D). At higher silica activities silica-bearing minerals are stable, either olivine (fayalite) or phyllosilicate (greenalite), while at the highest silica activities enstatite (ferrosilite) is predicted. In our experiments initial silica activities would have been very low (because high purity water was used). Concentrations would then increase only as Si-bearing minerals were dissolved. In CM chondrites much of the matrix was originally composed of amorphous GEMS phases which readily interacted with water, adding silica into solution (Leroux et al. 2015). By contrast, the mineralogy of our Kainsaz starting material is crystalline and therefore more resistant to dissolution. Observations under SEM show that (Mg-rich) chondrule silicates remained unaffected. These phases therefore donated negligible silica (and negligible Mg) to solution. Evidence for the chemical attack of feldspar (Fig. 1E) is present but relatively rare. This leaves the dissolution of micrometre-sized fayalite grains within the fine-grained matrix as the principal source of Si. Fig. 1 reveals how individual fayalite grains can be identified in the unaltered matrix. The altered matrix has a fused texture with a more uniform and finer-grain size. This is evidence for dissolution and reprecipitation of the matrix. The dissolution of fayalite (assuming an ideal end-member composition [Fe_2SiO_4]) would have added two atoms of Fe into solution for every atom of Si added. Furthermore, the vast amount of Fe added by the dissolution of kamacite means that Fe activities would have far outpaced silica activities and that, in absolute terms, silica activities would have remained low throughout the experiments. This is consistent with our observed alteration assemblages in which Fe-oxyhydroxides and Fe-oxide phases dominate, while Si-bearing phases (fayalite and/or Fe-rich phyllosilicate) formed at lower abundances. In the 50 °C samples fayalite (and potentially Si-bearing goethite [Gómez et al. 2011]) were the main Si-bearing phases formed, while in the 150 °C samples both fayalite and Fe-rich phyllosilicate formed.

The geochemical plot for the 150 °C system (Fig. 11D) shows that the fayalite stability field is highly restricted and lies at intermediate silica activities, in between the region of Fe-oxyhydroxides/oxide formation and phyllosilicate growth. This stability field is absent in the 50 °C plot (Fig. 11C), suggesting that hydrothermally formed fayalite may be prohibited. However, more detailed geochemical modelling specifically focusing on fayalite formation on chondritic asteroids by Zolotov et al. (2006) concluded that hydrothermally generated fayalite could occur at temperatures as low as 0 °C and at slightly elevated pressures (~3 bar). Under these conditions, Fe-rich end-member olivine compositions are favoured over Mg-bearing species.

5.5. The formation of new Fe-sulphide phases

Fe-sulphide phases in the unaltered Kainsaz are exclusively low-Ni (Ni < 0.2 at.%) with average (Fe + Ni)/S ratios of 0.98 ± 0.02 [1σ] (Fig. 6). They are members of the pyrrhotite-troilite sulphide group. Rare grains of exsolved pentlandite explain (Fe + Ni)/S ratios >1

(Francis et al., 1976; Schrader et al. 2021). By contrast, Fe-sulphides in the altered samples generally have elevated Ni abundances (<3.0 at.%) and lower average (Fe + Ni)/S ratios (50 °C: 0.98 ± 0.04 [1σ] and 150 °C: 0.92 ± 0.06). Because the size and spatial distribution of Fe-sulphides in the altered samples are similar to the unaltered Kainsaz, their elevated Ni concentrations (0.2 at.% < Ni < 3 at.%) are unlikely to have been produced by precipitation of new sulphide minerals. Instead, the altered sulphide compositions were most likely generated by solid state diffusion of Ni into the mineral structure from the fluid phase (Berger et al. 2016).

Schrader et al. (2021) demonstrated that sulphides in chondrites can be sensitive records of alteration conditions. They showed how Fe/S ratios can be used to infer the degree of oxidation, with lower ratios corresponding to more oxidising conditions. In our altered samples, the Fe/S ratios of low-Ni sulphides (average: 50 °C: 0.98 and 150 °C: 0.90) are similar to their combined (Fe + Ni)/S ratios. For the high temperature 150 °C sample these ratios are significantly lower than the starting composition (Fe/S ratio of the unaltered Kainsaz: 0.98), attesting to an oxidizing environment during alteration. Values between 0.90 and 0.93 overlap with the average sulphide compositions measured in the CM chondrites and also with the range measured in the anomalous CR Al Rais (Schrader et al. 2021). Furthermore, lower Fe/S ratios in the 150 °C samples (relative to the 50 °C samples), imply that the high-temperature experiments were more oxidizing.

In addition to solid state alteration of pre-existing sulphides (adding Ni and in the 150 °C samples lowering their (Fe + Ni)/S ratios), there is evidence for the precipitation of new nanophase Fe-sulphide minerals. As described in Section 3.3.4, their presence is inferred from the elevated S abundances detected in the fine-grained matrix of the altered samples (Fig. 2). Finally, a third population of Fe-sulphides can be distinguished. These are the high-Ni (Ni > 10 at.%) Fe-sulphides (pyrrhotites) that were found only in the 150 °C samples (Fig. 6). Their high Ni concentrations suggest that the precursor phase also contained high Ni abundances. As a result, sulphidation of taenite by fluids is the most likely origin for these minerals (Noguchi et al. 2011). The presence of high-Ni sulphides is significant because their presence is a diagnostic feature of the CV_{OX} subgroup (McSween, 1977a; Howard et al. 2010). Consequently, the formation of high-Ni sulphides in our experiments might explain the formation of Ni-rich sulphides in the oxidized CVs.

5.6. The formation of carbonates

Calcite grains were formed in all altered samples except sample Q. They occur at low abundances, being undetected in the XRD data but identifiable under SEM (Fig. 5D-5F) and in TGA plots (Fig. 7). Here the formation of calcite provides insights into the petrogenesis of carbonates on C-type asteroids.

Carbonates in hydrated carbonaceous chondrites formed during aqueous alteration by the geochemical reprocessing of either C-bearing ices (Alexander et al. 2015; Telus et al. 2019) and/or organic matter (Fujiya et al. 2015; 2020; Tyra et al. 2016; Vacher et al. 2017). The low-grade parent body metamorphic alteration that affected Kainsaz would have driven off volatile C-bearing ices and converted most organics into graphitized matter (Bonal et al. 2007; Remusat et al. 2008). As a result, C abundances in Kainsaz are low (<0.7 wt%, Greenwood and Franchi, 2004; Alexander et al. 2007) and far less than the abundances observed in pristine CO3 chondrites (~1.2 wt%, Alexander et al. 2018) and in most CM chondrites (between 1.0–2.2 wt%, Alexander et al. 2013). By using the C-poor Kainsaz as a starting material for our experiments we limited the potential of the hydrothermal system to form carbonates. However, because small quantities of calcite were formed this demonstrates that some of the remaining organic matter must have acted as a C donor during alteration.

We observed that calcite grains in our altered samples tend to form within void spaces inside chondrules. These voids were formed by the dissolution of kamacite. In Sample L, the early stages of calcite growth were imaged (Fig. 5E), showing growth developed as a meshwork texture, adhering to the walls of the voids. Thus, calcite precipitation occurred after the complete dissolution of the primary phases (as opposed to concurrent dissolution-precipitation). The preferential formation of calcite in chondrule voids may also reflect locally high Ca activities achieved by the dissolution of surrounding anorthite (Fig. 1E) or Ca-bearing pyroxene.

A single calcite grain found in sample A (Fig. 5F) had an unusual form. It is located within a chondrule but also decorated by a margin of Fe-sulphides. This texture is reminiscent of the T1 calcites found in CM chondrites, which contain a rim of mixed Fe-sulphides (tochilinite) and phyllosilicate (Lee et al. 2014; Lindgren et al. 2017; Vacher et al. 2017; 2019a). T1 calcites formed early in the CM chondrite alteration sequence, at relatively low temperatures (<70 °C, Guo and Eiler, 2007; Vacher et al. 2019a) and prior to widespread phyllosilicate-sulphide growth. By contrast, the calcite grain in Sample A – although superficially similar to T1 calcites – has a different petrogenesis. Because this calcite grain formed within a chondrule void its growth is analogous to vein formation where minerals grow progressively from the outer edge inwards. Cross-cutting relationships therefore require that the Fe-sulphides formed first, while the calcite precipitated later. This is the reverse of the order for T1 calcites in CM chondrites (calcite then Fe-sulphides). Calcite formed after Fe-sulphide formation.

Calcite formation is dependent on both dissolved Ca^{2+} and CO_3^{2-} activities, as well as pH. Alkaline conditions facilitate the precipitation of calcite at lower Ca^{2+} activities (Fig. 11E and F). At the onset of alteration, Ca^{2+} activities would be at zero and pH conditions are expected to have been neutral. The alteration environment would have transitioned to higher pH (more alkaline), primarily driven by the dissolution of kamacite and corresponding loss of H^+ ions from solution. At the same time, the abundance of Ca^{2+} and CO_3^{2-} ions would slowly increase as Ca-bearing feldspars and pyroxenes were dissolved and organics were

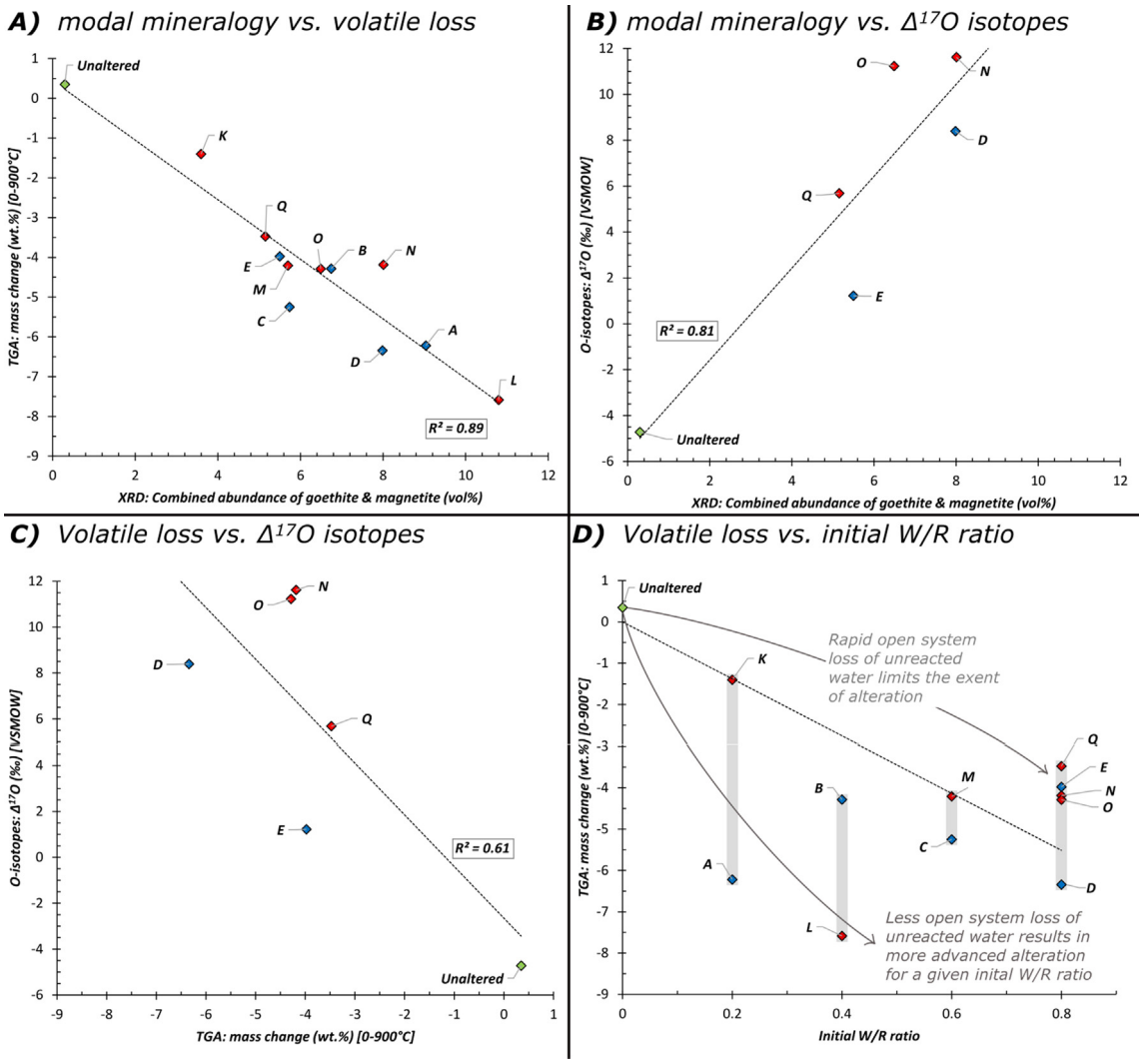

Fig. 12. Inferring the extent of aqueous alteration and exploring its relationship with O-isotope composition. Panel A compares the abundance of Fe-oxyhydroxides/oxides (magnetite + goethite) against the amount of released volatiles from the TGA analyses. A robust linear correlation ($R^2 = 0.89$) demonstrates that both metrics agree and are effective at determining the relative extent of alteration. Sample K is least altered while sample L is most altered. Panel B compares the abundance of Fe-oxyhydroxides/oxides against the $\Delta^{17}O$ isotope composition, revealing a positive linear correlation ($R^2 = 0.81$), demonstrating that more advanced alteration corresponds to more ^{17}O-enriched compositions and confirming that secondary phases are carriers of the isotopically doped heavy water. Panel C compares TGA volatile loss against $\Delta^{17}O$ isotope composition, showing a negative linear correlation ($R^2 = 0.61$) as further support that extent of alteration and O-isotope composition are linked. Panel D compares volatile loss (as a proxy for alteration extent) against a sample's initial W/R_E ratio. In general, high-temperature samples have more ^{17}O-enriched compositions for a given degree of alteration. This reflects the competing effects of extent of alteration and loss of isotopically light water (due to open system behaviour) on the sample's final bulk O-isotope composition.

oxidized. At some point the environmental conditions transitioned to the region of calcite stability (Fig. 11E and F), leading to precipitation. Since calcites formed late in the alteration sequence these conditions approximately correspond to the final fluid compositions.

5.7. Comparing the style and extent of alteration

Alteration style was similar in all 11 experiments. The main changes observed are the widespread dissolution of Fe-Ni-metal and formation of Fe-oxyhydroxides (primarily goethite). These formed several distinct morphologies, including (i) large, layered growth structures, (ii) abundant thin sinuous veins that cut through the matrix and fractured anhydrous silicates and (iii) dense regions of Fe-enriched matrix (Figs. 3 and 5). New nanophase Fe-sulphide grains were formed within the fine-grained matrix of all the altered rock chips (samples A-O). Meanwhile, pre-existing sulphides were altered by increases in their Ni content. Exclusive to the 150 °C samples pre-existing sulphides were partially oxidized, lowering their (Fe + Ni)/S ratios and an entirely new generation of Ni-rich sulphides were also formed, possibly by the alteration of taenite. There is some evidence for fayalite formation occurring within the fine-grained matrix (Fig. 3E and F). This is best demonstrated by the presence of localized regions containing large,

interlocking grains with a crystalline texture (distinct from the fluffy texture in the unaltered Kainsaz). Accessory phases include carbonates and sulphate masses (Fig. 5B). Limited quantities of poorly crystalline and fine-grained phyllosilicate were formed in the 150 °C samples that started with W/R_E ratios >0.2 (Fig. 8 and S4).

Fe-oxyhydroxides and Fe-oxides were the dominant secondary minerals formed. As the unaltered Kainsaz contains no Fe-oxyhydroxides and minimal magnetite (~0.3 vol%), the abundance of these phases in the altered samples inferred from the modal mineralogy (Table S2) or volatile phases released during TGA (Fig. 7 and Table S3) can therefore be used to estimate the relative extent of alteration. Comparing the two datasets reveals a statistically robust negative correlation (R^2 = 0.89, Pearson = -0.94, p-value: 4.3E-06, Fig. 12A). Higher abundances of goethite and magnetite correspond closely to larger quantities of evolved volatile gases. The sequence of alteration spans from Sample K as least altered to Sample L as most altered. A tight cluster of samples show similar degrees of alteration (Q, E, M, O, B, C and N), while samples D, A and L are more extensively altered.

Our experiments included a powdered sample (Q). Based on the XRD or TGA metrics (Fig. 12A) sample Q appears to have experienced relatively modest alteration, being more altered than (the least altered) sample K and similar to samples E, M and O. This is surprising given the expectation that the larger surface area would have promoted faster reaction rates and therefore resulted in a more advanced alteration extent. However, alteration may have been limited by early water loss from the reaction vessel thereby lowering the effective W/R_E ratio.

Comparing the relationship between W/R_E ratio and extent of alteration (Fig. 12D) reveals a weak correlation, in which higher initial water abundances correspond to more advanced alteration. However, because variable and unquantified open system behaviour (Section 4.1) affected our experiments the relationship between W/R_E ratio and extent of alteration cannot be determined more accurately.

Alteration was dominated by fluid mediated Fe and, to a lesser extent S mobilization and redeposition under alkaline and moderately oxidizing conditions. The style of alteration in our experiments is best described as Fe-alkali metasomatism. The altered samples show similarities to both the CV and CM chondrites. Parallels with the alteration in CV chondrites can be seen in the development of fayalite within the fine-grained matrix and the formation of Ni-bearing Fe-sulphides. Conversely, similarities to the CM chondrites include the formation of (Fe-rich) phyllosilicates, the presence of Fe-rich aureole structures (Fig. 3A and B) similar to those described in Hanowski and Brearley (2000), and the formation of calcite.

5.8. The sequence of mineralisation

Because the style of alteration was similar, we can reconstruct the approximate sequence of mineralization (Fig. 13) using cross-cutting relationships and by comparing samples with different alteration extents. The first minerals to form (inferred by their presence even in the least altered sample [K]) would have been Fe-oxyhydroxides/oxides precipitating rapidly after kamacite dissolution (Section 4.3). However, we also argued that, to produce extensive redistribution of Fe, as observed in the most altered samples

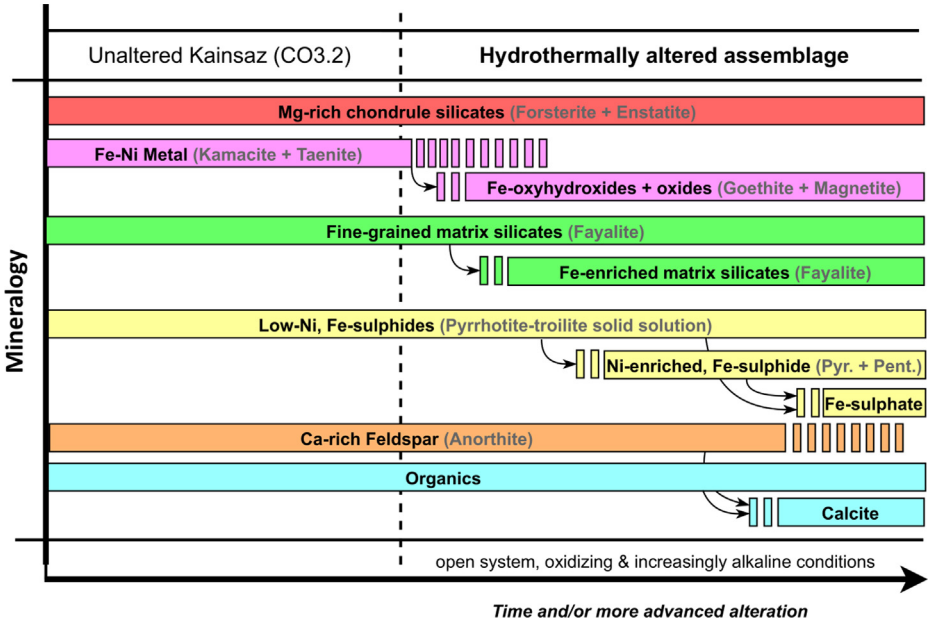

Fig. 13. Schematic sketch illustrating the qualitative style of alteration observed in this study and how primary and secondary phases are related. On the left, the unaltered Kainsaz mineralogy transitions into the hydrothermally altered assemblage (displayed on the right). The passage of time and correspondingly more advanced alteration is shown on the x-axis, allowing the approximate sequence of mineralization to be visualised. Note, this diagram does not attempt to display relative mineral abundances.

(e.g. Samples A, C, D and L), would have required a prolonged period of dissolution and precipitation, thus, Fe-oxyhydroxides/oxide formation likely continued while liquid water remained available.

All the altered samples have regions of fine-grained matrix that are S-enriched (Fig. 2), suggesting that Fe-sulphide mobilization and reprecipitation, forming nano-scale grains occurred early in the alteration sequence. This is supported by observations of early sulphide formation in minimally altered CM chondrites (Palmer and Lauretta, 2011; Leroux et al. 2015; Pignatelli et al. 2017). By contrast, the formation of larger Fe-sulphide grains, such as the micrometre-scale sulphides measured in Fig. 3C and D would have required longer to grow.

The most obvious examples of new fayalite formation (Fig. 3E and F) are found in the low-temperature experiments, including those where residual water remained at the end of the experiments. However, when, and to what extent fayalite formed (or existing grains grew larger) is difficult to discern. This is because the unaltered Kainsaz starting mineralogy is composed of (fine-grained) fayalite crystals and it is not always clear which fayalite grains are of parent body origin and which crystals were produced during experimental alteration. As such, the window of fayalite growth is poorly constrained but estimated to be after Fe-oxyhydroxides/oxide formation.

Phyllosilicates (which were detected in the 150 °C samples) could form only once silica activities reached sufficiently high concentrations. This would have required the dissolution of matrix silicates and therefore constrains phyllosilicate growth to a relatively late feature, likely coincident with, or after fayalite formation. Their absence in the low-temperature samples, even where liquid water remained at the end of the experiments supports this conclusion.

Cross-cutting relationships (Section 4.6) require that calcite formed relatively late, after Fe-sulphides. Calcite formation was inhibited by low abundances of Ca^{2+} ions, most likely a consequence of slow rates of feldspar and pyroxene dissolution. However, as alteration advanced and water was lost from the reaction vessel or consumed in alteration reactions, any Ca^{2+} ions in solution would become passively concentrated. This effect may have facilitated calcite growth. Finally, because Fe-sulphate was found in only the most altered samples implies this phase formed late in the alteration sequence.

5.9. The O-isotopic perspective

Aqueous alteration on chondritic asteroids was characterized by the exchange between isotopically light (^{16}O-rich) anhydrous minerals and isotopically heavy (^{16}O-poor) water, leading to the formation of new secondary phases with intermediate compositions (Rowe et al. 1994; Clayton and Mayeda, 1999; Yurimoto et al. 2008; Suttle et al. 2021a). Our hydrothermal experiments attempted to reproduce this behaviour using water with an isotopically heavy and distinctive signature (δ^{17}O: +64.49‰, δ^{18}O: −3.92‰, Morris, 2008). Measurement of the altered rock compositions aimed to determine the magnitude of any mass fractionation effects and the amount of isotopic exchange.

Five samples were reacted with the doped water (samples D, E, N, O and Q). They all have elevated Δ^{17}O values relative to their starting compositions (Fig. 9A). In addition, we observe a robust correlation between the extent of aqueous alteration (inferred from XRD or TGA) and O-isotope compositions (Fig. 12B and C). This relationship was expected and demonstrates that mixing (isotopic exchange) occurred between the rock and doped water (Fig. 9B).

Theoretically, in a closed system after the entire water fraction has reacted, the final bulk O-isotope composition of the altered samples should plot somewhere on a tie-line linking the initial rock and initial water compositions (marked by the dotted black line in Fig. 9A). A sample's position on this tie-line reflects the effective W/R ratio of the system (Clayton and Mayeda, 1999). Most of our altered samples (D, N, O and Q) plot relatively close to this tie-line but not on the line. Instead, their compositions are shifted in δ^{18}O space, having migrated to heavier ^{18}O-enriched values (with the exception of sample E, whose composition has shifted to lighter values [discussed below]). Mass fractionation to heavier compositions can be achieved if some of the initial water remained unreacted, either because the experiments were terminated early (i.e. water remained when the vessels were opened), or because some of the water escaped the system during the experiment. Both these scenarios occurred in our experiments. We noted in Section 3.1. that samples D and E retained a small amount of residual liquid water at the end of their experiments (Fig. S1B). In addition, evidence from mass balance arguments (Section 4.2) suggests that all the experiments operated as partially open systems with the slow released of water vapour. In the case of open system loss, water molecules containing light oxygen (^{16}O) will preferentially escape, resulting in mass-dependent fractionation of the remaining water to heavier compositions. This water then continued to react with the rock. In the triple O-isotope system mass fractionation follows a slope 0.52 line (Clayton and Mayeda, 1999). Consequently, the escape of water from the vessels would have left the remaining water to fractionate along a 0.52 slope (parallel to the TFL, as shown in Fig. 9B).

In addition to mixing and mass fractionation of the remaining water, a third isotopic effect acted on this system. Secondary minerals formed during aqueous alteration do not directly sample the isotopic composition of the fluid from which they formed. Instead, they are affected by temperature-dependent mass fractionation. This process is described by a "*fractionation factor*" (denoted by the α symbol) which quantifies the relationship between precipitated mineral and the host water compositions at a given temperature (Becker and Clayton, 1976; Verdier-Paoletti et al. 2017; Jilly-Rehak et al. 2018). Fractionation effects are greatest at low temperatures and exponentially decrease in magnitude with rising temperature. The main alteration minerals formed in this study were goethite and magnetite. Both form with isotopically lighter compositions than the fluids from which they precipitate. Although the effect is

more extreme for magnetite (Becker and Clayton, 1976; Yong-fei, 1991; Jilly-Rehak et al. 2018) than it is for goethite (Yapp, 1990; Bao and Koch, 1999).

Previously we noted that sample E had a composition that plots to the left of the tie-line in Fig. 9A (lower $\delta^{18}O$ values than the rest of the samples). This position could be produced if the main window of secondary mineralization occurred prior to significant open system water loss, resulting in fractionation between mineral and the lightest possible water composition. Alternatively, the relatively light isotopic composition in sample E may reflect an experiment in which only a small amount of water was lost from the system (less than in the other experiments). This is consistent with the observation that sample E retained the largest amount of residual water at the end of the experiment (Section 3.1, Fig.S1B).

In contrast, to the low-temperature samples, the higher temperature samples (N, O and Q) have heavier compositions, indicating more pronounced mass fractionation effects arising due to open system water loss (Fig. 9B). This implies that the secondary mineralization in the high temperature samples predominantly occurred after a significant fraction of the initial water had escaped.

Collectively the isotopic evidence hints at two divergent alteration pathways, with the low temperatures samples most likely experiencing aqueous alteration followed by progressive water loss, while the high temperature samples lost a significant fraction of their initial water early in the experiment before aqueous alteration advanced. These differing trajectories would have exaggerated the differences between low temperature aqueous alteration in samples A-E and a drier, warmer metasomatic environment in samples K-Q.

6. IMPLICATIONS

6.1. Departures from CM-like alteration and suggested revisions for a future experimental design

We set out to test if aqueous alteration of a CO chondrite under conditions similar to those predicted for the CM chondrites would produce a CM-like mineral assemblage. Our altered samples shared some similarities with CM chondrites; namely the formation of carbonates, sulphates, magnetite, goethite and (limited quantities of) phyllosilicate as well as the generation of Fe-rich halo structures. Overall however, the altered samples do not bear strong similarities to CM chondrites. Instead, they record an Fe-alkali metasomatic environment, similar to the conditions that affected the CV chondrites (Krot et al. 1998; 2004; Bonal et al. 2020).

The absence of tochilinite and the lack (or low abundance) of cronstedtite are the greatest differences between our experiments and CM alteration. Previous studies argued that reducing environments were required for the development of these two quintessential CM chondrite minerals (Harder, 1978; Peng et al. 2009; Peng and Jing, 2014; Vacher et al. 2019b). Our experimental work supports those conclusions, confirming that tochilinite and cronstedtite growth (and therefore TCI structures) are inhibited under oxidizing conditions. However, the advanced stages of CM alteration were oxidizing (Suttle et al. 2021a) as demonstrated by the destruction of organics in CM1 chondrites (Botta et al. 2007), lower Fe/S ratios in sulphides from more heavily altered CMs (Schrader et al. 2021), higher abundances of magnetite in more heavily altered CMs (King et al. 2017), the conversion of cronstedtite to polyhedral serpentine (Zega et al. 2006) and the late-stage formation of gypsum (Lee et al. 2014). Our experiments therefore mimicked the environmental conditions during the advanced stages of alteration on the CM parent body. Furthermore, although most evidence points towards isochemical closed system alteration (Clayton and Mayeda, 1999; Benedix et al., 2003; Bland et al. 2009) our open system experiments may be appropriate analogous for near-surface conditions on the CM parent body where evolved gases (such as H_2 and CH_4) could escape into space (e.g. Guo and Eiler, 2007; Le Guillou et al. 2015).

Below we outline three principal reasons why alteration differed from a CM-like trajectory and how a revised experimental design could more closely reproduce a CM environment across the entire alteration pathway (e.g. initially reducing and progressively evolving to oxidising):

(1) ***Choice of starting mineralogy:*** The matrix of the most primitive CCs (Le Guillou et al., 2015), including the CO chondrites (McAdam et al. 2018; Alexander et al. 2018; Davidson et al. 2019; Bonato, 2020) and the least-altered CM chondrites (Leroux et al. 2015; Kimura et al. 2020) are composed of amorphous GEMS-like phases. Several experimental studies have shown how these amorphous phases readily convert to phyllosilicates on contact with water (Nelson et al., 1987; Rietmeijer et al., 2004; Nakamura-Messenger et al. 2011; Takigawa et al., 2019). By contrast, our starting material was a CO3.2 chondrite that had experienced an episode of post-accretion thermal metamorphism with peak temperatures between 300 °C and 400 °C (Scott and Jones, 1990; Huss and Lewis, 1994; Busemann et al. 2007). Metamorphism led to the crystallization of glass (Tomeoka and Itoh, 2004), the crystallization of amorphous silicate within the matrix (Bonato, 2020), the coarsening of nanophase matrix sulphides into larger grains (Grossman and Brearley, 2005) and the loss of organics (Bonal et al. 2007; Remusat et al. 2008). These effects made Kainsaz more resistant to aqueous alteration by replacing amorphous phases (matrix silicates and chondrule glass) with crystalline phases (fayalite and mixed nepheline/plagioclase respectively) and by lowering the carbon budget, which limited carbonate formation (Section 4.6). This had the effect of delaying the onset of phyllosilicate formation. From the outset, our alteration conditions produced higher dissolved Fe abundances and lower dissolved Si abundances (due to the dissolution of kamacite without concurrent silicate dissolution) that would have imparted a strong control on the style of alteration as reactions advanced. Ideally,

future experiments should use a more primitive CO chondrite, containing amorphous matrix material to test this hypothesis.

(2) ***Unplanned open system gas loss***: The unplanned loss of gases from reaction vessels meant that alteration conditions were open system (Section 5.2). This lowered the effective W/R ratios, pushing conditions from an aqueous alteration environment into a drier metasomatic environment. Limited water meant that solutions were more readily saturated and therefore that high salinity environments prevailed. These are not effective at dissolving silicates (Lamadrid et al., 2017). This most likely explains why we did not observe dissolution of Mg-rich chondrule silicates. Consequently, dissolved Si activities remained low (Section 5.4), inhibiting phyllosilicate formation (Fig. 11C and D).

(3) ***Oxygen fugacity, oxidizing conditions***: Finally, because our experiments contained a small initial quantity of O_2 in the reaction vessel headspace this would have promoted oxidizing conditions. (Later, open system escape of H_2 gas produced in the oxidation of metal was likely an even more significant cause of oxidizing conditions). Since the early formation of tochilinite and cronstedtite requires reducing conditions (Shipko and Douglas, 1956; Harder, 1978; Peng and Jing, 2014; Vacher et al. 2019b) this initial headspace negatively impacted the experiment's aim.

To resolve these problems future experiments could use a more pristine CO chondrite (ideally a CO3.00 [such as DOM 08006]), change the type of reaction vessels, to prevent gas escape and fill the reaction vessel headspace with an inert gas, such as an argon.

6.2. Consequences for the CO-CM relationship

The idea that the CO and CM chondrites formed on a single parent body appears unsupported by most data (Schrader and Davidson, 2017; Chaumard et al., 2018; Kimura et al. 2020). However, their close relationship, particularly in terms of refractory silicates and bulk O-isotope compositions remains clear. The CO-CM clan most likely represents asteroids formed from the same reservoir or region of the protoplanetary disk but at different times (Sugiura and Fujiya, 2014; Chaumard et al., 2018).

The primary difference between the CO and CM chondrites was the amount of initial water they accreted. However, the CM chondrites are more than simply wet CO chondrites. Our experiments demonstrated that addition of water and alteration under oxidizing conditions produces some similarities to a CM chondrite mineralogy, but fundamental phases (tochilinite, cronstedtite and TCIs) are missing. We conclude that a crystalline matrix was the main reason why Kainsaz did not evolve towards a CM-like assemblage. As a result, although Lee et al. (2019a) observed evidence of pre-hydration alkali-halogen metasomatism in the CM chondrite MET 01,075 our experiments define an upper limit to the amount of early thermal alteration that could have occurred – namely that widespread crystallization of amorphous GEMS-like materials was avoided. Conversely, the mildly metamorphosed Kainsaz proved to be a suitable analogue for the protolith material of the CV parent body.

7. CONCLUSIONS

Our hydrothermal experiments operated under alkaline and oxidising conditions, producing an Fe-alkali metasomatic style of alteration. This is most similar to conditions that affected the oxidized CV chondrites but also bears similarities to the oxidizing environment that existed on CM chondrite parent body during late-stage aqueous alteration. Although unplanned, open system gas loss is potentially relevant to near-surface conditions on primitive asteroids. The dissolution of kamacite and to a lesser extent anorthite, fayalite and sulphides facilitated the formation of a diverse range of secondary minerals: goethite, magnetite, fayalite, Ni-bearing Fe-sulphides, Fe-rich phyllosilicates, Fe-sulphate and calcite. Reconstructing the approximate sequence of mineralisation revealed that Fe-oxyhydroxides/oxides and Fe-sulphides formed early while phyllosilicates were slow to grow, inhibited by low silica activities. Late-stage minerals include Ni-rich sulphides, Fe-sulphate and calcite. Alteration textures in the low-temperature samples closely mirror the Fe-rich haloes and aureoles described by Hanowski and Brearley (2000) from three CM chondrites and by Haenecour et al. (2020) in the ungrouped CO-like chondrite MIL 07687. These may be evidence of restricted geochemical microenvironments, reflecting a system in which fluids rapidly reacted with matrix. By contrast, the high-temperature experiments produced more CV-like features, notably the generation of Ni-rich sulphides, probably by sulphidation of taenite under oxidizing conditions. This may reflect how the diagnostic Ni-rich sulphides were generated in the CVs.

The use of isotopically doped water produced altered samples with $\Delta^{17}O$-enriched compositions, reflecting isotopic mixing between rock and water. The low temperature samples show evidence of ^{18}O-depleted compositions, we interpret this reflecting the formation of isotopically light magnetite and goethite minerals before significant water loss. By contrast, the high-temperature samples have ^{18}O-enriched compositions, reflecting a system in which a significant fraction of the initial water escaped the reaction vessel before aqueous alteration advanced. Despite these complex effects, our data demonstrate that more advanced alteration is closely correlated to higher initial W/R_E ratios.

Declaration of Competing Interest

The authors declare that they have no known competing financial interests or personal relationships that could have appeared to influence the work reported in this paper.

ACKNOWLEDGEMENTS

This research was funded the Science and Technology Facilities Council (STFC), UK, through grant ST/R000727/1, *The Geological History of Water-rich Asteroids*. We thank STFC for a grant extension that allowed this work to be completed after delays due to the COVID-19 pandemic. We thank Susanne Schwenzer at the OU for her helpful discussions on geochemical modeling. At the NHM we thank Nicola Laing, Caroline Coleman and Alex Ball for their logistical support and Callum Hatch for sample preparation. We are grateful to Yves Marrocchi for editorial handling as well as Lionel Vacher, Wataru Fujiya and an anonymous reviewer for their insightful comments during the review process.

APPENDIX A. SUPPLEMENTARY MATERIAL

Supplementary data to this article can be found online at https://doi.org/10.1016/j.gca.2021.11.028.

REFERENCES

Alexander C. O. D., Fogel M., Yabuta H. and Cody G. D. (2007) The origin and evolution of chondrites recorded in the elemental and isotopic compositions of their macromolecular organic matter. *Geochim Cosmochim. Acta* **71**, 4380–4403.

Alexander C. M. D., Howard K. T., Bowden R. and Fogel M. L. (2013) The classification of CM and CR chondrites using bulk H, C and N abundances and isotopic compositions. *Geochim. Cosmochim. Acta* **123**, 244–260.

Alexander C. O. D., Bowden R., Fogel M. L. and Howard K. T. (2015) Carbonate abundances and isotopic compositions in chondrites. *Meteorit. Planet. Sci.* **50**, 810–833.

Alexander C. M. D., Greenwood R. C., Bowden R., Gibson J. M., Howard K. T. and Franchi I. A. (2018) A mutli-technique search for the most primitive CO chondrites. *Geochim. Cosmochim. Acta* **221**, 406–420.

Ahrens L. H., Willis J. P. and Erlank A. J. (1973) The chemical composition of Kainsaz and Efremovka. *Meteoritics* **8**, 133–139.

Bao H. and Koch P. L. (1999) Oxygen isotope fractionation in ferric oxide-water systems: low temperature synthesis. *Geochim. Cosmochim. Acta* **63**, 599–613.

Becker R. H. and Clayton R. N. (1976) Oxygen isotope study of a Precambrian banded iron-formation, Hamersley Range, Western Australia. *Geochim. Cosmochim. Acta* **40**, 1153–1165.

Benedix G. K., Leshin L. A., Farquhar J., Jackson T. and Thiemens M. H. (2003) Carbonates in CM2 chondrites: Constraints on alteration conditions from oxygen isotopic compositions and petrographic observations. *Geochim. Cosmochim. Acta* **67**, 1577–1588.

Berger E. L., Lauretta D. S., Zega T. J. and Keller L. P. (2016) Heterogeneous histories of Ni-bearing pyrrhotite and pentlandite grains in the CI chondrites Orgueil and Alais. *Meteorit. Planet. Sci.* **51**, 1813–1829.

Beverskog B. and Puigdomenech I. (1996) Revised pourbaix diagrams for iron at 25–300 C. *Corros. Sci.* **38**, 2121–2135.

Bland P. A., Jackson M. D., Coker R. F., Cohen B. A., Webber J. B. W., Lee M. R., Duffy C. M., Chater R. J., Ardakani M. G., McPhail D. S. and McComb D. W. (2009) Why aqueous alteration in asteroids was isochemical: High porosity≠ high permeability. *Earth Planet. Sci. Lett.* **287**, 559–568.

Bonal L., Bourot-Denise M., Quirico E., Montagnac G. and Lewin E. (2007) Organic matter and metamorphic history of CO chondrites. *Geochim. Cosmochim. Acta* **71**, 1605–1623.

Bonal L., Gattacceca J., Garenne A., Eschrig J., Rochette P. and Ruggiu L. K. (2020) Water and heat: New constraints on the evolution of the CV chondrite parent body. *Geochim. Cosmochim. Acta* **276**, 363–383.

Bonato, E., (2020). From Protoplanetary Dust to Asteroidal Heating: A mineralogical study of the CO3 chondrites. (Doctoral dissertation, Glasgow University). Avaliable at: http://theses.gla.ac.uk/81952/

Botta O., Martins Z. and Ehrenfreund P. (2007) Amino acids in Antarctic CM1 meteorites and their relationship to other carbonaceous chondrites. *Meteorit. Planet. Sci.* **42**, 81–92.

Bradley J. P. (1994) Chemically anomalous, preaccretionally irradiated grains in interplanetary dust from comets. *Science* **265**, 925–929.

Bradley J. P. (2019) GEMS and the devil in their details. *Nat. Astron.* **3**, 603–605.

Brearley A. J. (1995) Aqueous alteration and brecciation in Bells, an unusual, saponite-bearing, CM chondrite. *Geochim. Cosmochim. Acta* **59**, 2291–2317.

Brearley A. J. (2006) The action of water. *Meteorit. Early Solar Syst. II* **943**, 587–624.

Brearley A. J. and Krot A. N. (2013) Metasomatism in the early solar system: The record from chondritic meteorites. In *Metasomatism and the Chemical Transformation of Rock*. Springer, Berlin, Heidelberg, pp. 659–789.

Brearley A. J. and Jones R. H. (2018) Halogens in chondritic meteorites. In *The Role of hhalogens in Terrestrial and Extraterrestrial Geochemical Processes*. Springer, Cham, pp. 871–958.

Bridges J. C., Schwenzer S. P., Leveille R., Westall F., Wiens R. C., Mangold N., Bristow T., Edwards P. and Berger G. (2015) Diagenesis and clay mineral formation at Gale Crater, Mars. *J. Geophys. Res. Planets* **120**, 1–19.

Browning L. B., McSween, Jr, H. Y. and Zolensky M. E. (1996) Correlated alteration effects in CM carbonaceous chondrites. *Geochim. Cosmochim. Acta* **60**, 2621–2633.

Busemann H., Alexander M. O. D. and Nittler L. R. (2007) Characterization of insoluble organic matter in primitive meteorites by microRaman spectroscopy. *Meteorit. Planet. Sci.* **42**, 1387–1416.

Changela H. G. and Bridges J. C. (2010) Alteration assemblages in the nakhlites: Variation with depth on Mars. *Meteorit. Planet. Sci.* **45**, 1847–1867.

Chaumard N., Defouilloy C. and Kita N. T. (2018) Oxygen isotope systematics of chondrules in the Murchison CM2 chondrite and implications for the CO-CM relationship. *Geochim. Cosmochim. Acta* **228**, 220–242.

Clayton R. N. and Mayeda T. K. (1999) Oxygen isotope studies of carbonaceous chondrites. *Geochim. Cosmochim. Acta* **63**, 2089–2104.

Cressey G. and Schofield P. F. (1996) Rapid whole-pattern profile-stripping method for the quantification of multiphase samples. *Powder Diffr.* **11**, 35–39.

Davidson J., Alexander C. M. D., Stroud R. M., Busemann H. and Nittler L. R. (2019) Mineralogy and petrology of Dominion Range 08006: A very primitive CO3 carbonaceous chondrite. *Geochim. Cosmochim. Acta* **265**, 259–278.

Doyle P. M., Jogo K., Nagashima K., Krot A. N., Wakita S., Ciesla F. J. and Hutcheon I. D. (2015) Early aqueous activity on the ordinary and carbonaceous chondrite parent bodies recorded by fayalite. *Nat. Commun.* **6**, 1–10.

Ebel D. S., Brunner C., Konrad K., Leftwich K., Erb I., Lu M., Rodriguez H., Crapster-Pregont E. J., Friedrich J. M. and Weisberg M. K. (2016) Abundance, major element composition and size of components and matrix in CV, CO and Acfer 094 chondrites. *Geochim. Cosmochim. Acta* **172**, 322–356.

Edwards G. H. and Blackburn T. (2020) Accretion of a large LL parent planetesimal from a recently formed chondrule population. *Sci. Adv.* **6**, p.eaay8641.

Filiberto J. and Schwenzer S. P. (2013) Alteration mineralogy of Home Plate and Columbia Hills-Formation conditions in context to impact, volcanism, and fluvial activity. *Meteorit. Planet. Sci.* **48**, 1937–1957.

Francis C. A., Fleet M. E., Misra K. and Craig J. R. (1976) Orientation of exsolved pentlandite in natural and synthetic nickeliferous pyrrhotite. *Am. Mineral.* **61**, 913–920.

Fujiya W., Sugiura N., Hotta H., Ichimura K. and Sano Y. (2012) Evidence for the late formation of hydrous asteroids from young meteoritic carbonates. *Nat. Commun.* **3**, 1–6.

Fujiya W., Sugiura N., Marrocchi Y., Takahata N., Hoppe P., Shirai K., Sano Y. and Hiyagon H. (2015) Comprehensive study of carbon and oxygen isotopic compositions, trace element abundances, and cathodoluminescence intensities of calcite in the Murchison CM chondrite. *Geochim. Cosmochim. Acta* **161**, 101–117.

Fujiya W., Aoki Y., Ushikubo T., Hashizume K. and Yamaguchi A. (2020) Carbon isotopic evolution of aqueous fluids in CM chondrites: Clues from in-situ isotope analyses within calcite grains in Yamato-791198. *Geochim. Cosmochim. Acta* **274**, 246–260.

Ganino C. and Libourel G. (2017) Reduced and unstratified crust in CV chondrite parent body. *Nat. Commun.* **8**, 1–10.

Ganino C. and Libourel G. (2020) Fumarolic-like activity on carbonaceous chondrite parent body. *Sci.* **6**, p.eabb1166.

Garenne A., Beck P., Montes-Hernandez G., Chiriac R., Toche F., Quirico E., Bonal L. and Schmitt B. (2014) The abundance and stability of "water" in type 1 and 2 carbonaceous chondrites (CI, CM and CR). *Geochim. Cosmochim. Acta* **137**, 93–112.

Gattacceca J., Bonal L., Sonzogni C. and Longerey J. (2020) CV chondrites: More than one parent body. *Earth Planet. Sci. Lett.* **547** 116467.

Greenwood R. C. and Franchi I. A. (2004) Alteration and metamorphism of CO3 chondrites: Evidence from oxygen and carbon isotopes. *Meteorit. Planet. Sci.* **39**, 1823–1838.

Greenwood R. C., Burbine T. H. and Franchi I. A. (2020) Linking asteroids and meteorites to the primordial planetesimal population. *Geochim. Cosmochim. Acta* **277**, 377–406.

Grossman J. N. and Brearley A. J. (2005) The onset of metamorphism in ordinary and carbonaceous chondrites. *Meteorit. Planet. Sci.* **40**, 87–122.

Gómez J. M., De Resende V. G., Antonissen J. and De Grave E. (2011) Characterization of the effects of silicon on the formation of goethite. *Corros. Sci.* **53**, 1756–1761.

Guo W. and Eiler J. M. (2007) Temperatures of aqueous alteration and evidence for methane generation on the parent bodies of the CM chondrites. *Geochim. Cosmochim. Acta* **71**, 5565–5575.

Haar L. (1984) *NBS/NRC steam tables*. CRC Press.

Haenecour P., Floss C., Brearley A. J. and Zega T. J. (2020) The effects of secondary processing in the unique carbonaceous chondrite Miller Range 07687. *Meteorit. Planet. Sci.* **55**, 1228–1256.

Hanowski N. P. and Brearley A. J. (2000) Iron-rich aureoles in the CM carbonaceous chondrites Murray, Murchison, and Allan Hills 81002: Evidence for in situ aqueous alteration. *Meteorit. Planet. Sci.* **35**, 1291–1308.

Harder H. (1978) Synthesis of iron layer silicate minerals under natural conditions. *Clays Clay Miner.* **26**, 65–72.

Holland T. J. B. and Powell R. (2011) An improved and extended internally consistent thermodynamic dataset for phases of petrological interest, involving a new equation of state for solids. *J. Metamorph. Geol.* **29**, 333–383.

Howard K. T., Benedix G. K., Bland P. A. and Cressey G. (2009) Modal mineralogy of CM2 chondrites by X-ray diffraction (PSD-XRD). Part 1: Total phyllosilicate abundance and the degree of aqueous alteration. *Geochim. Cosmochim. Acta* **73**, 4576–4589.

Howard K. T., Benedix G. K., Bland P. A. and Cressey G. (2010) Modal mineralogy of CV3 chondrites by X-ray diffraction (PSD-XRD). *Geochim. Cosmochim. Acta* **74**, 5084–5097.

Howard K. T., Benedix G. K., Bland P. A. and Cressey G. (2011) Modal mineralogy of CM chondrites by X-ray diffraction (PSD-XRD): Part 2. Degree, nature and settings of aqueous alteration. *Geochim. Cosmochim. Acta* **75**, 2735–2751.

Howard K. T., Alexander C. O. D., Schrader D. L. and Dyl K. A. (2015) Classification of hydrous meteorites (CR, CM and C2 ungrouped) by phyllosilicate fraction: PSD-XRD modal mineralogy and planetesimal environments. *Geochim. Cosmochim. Acta* **149**, 206–222.

Hua X. and Buseck P. R. (1995) Fayalite in the Kaba and Mokoia carbonaceous chondrites. *Geochim. Cosmochim. Acta* **59**, 563–578.

Huss G. R. and Lewis R. S. (1994) Noble gases in presolar diamonds II: Component abundances reflect thermal processing. *Meteorit.* **29**, 811–829.

Ivanova M. A., Lorenz C. A., Franchi I. A., Bychkov A. Y. and Post J. E. (2013) Experimental simulation of oxygen isotopic exchange in olivine and implication for the formation of metamorphosed carbonaceous chondrites. *Meteorit. Planet. Sci.* **48**, 2059–2070.

Janssens M. L. (2011) Thermogravimetric study of dehydration and thermal degradation of gypsum board at elevated temperatures. *Fire Saf. Sci.* **10**, 295–306.

Jilly-Rehak C. E., Huss G. R., Nagashima K. and Schrader D. L. (2018) Low-temperature aqueous alteration on the CR chondrite parent body: Implications from in situ oxygen-isotope analyses. *Geochim. Cosmochim. Acta* **222**, 230–252.

Jogo K., Nakamura T., Noguchi T. and Zolotov M. Y. (2009) Fayalite in the Vigarano CV3 carbonaceous chondrite: Occurrences, formation age and conditions. *Earth Planet. Sci. Lett.* **287**, 320–328.

Jogo K., Nakamura T., Ito M., Wakita S., Zolotov M. Y. and Messenger S. R. (2017) Mn–Cr ages and formation conditions of fayalite in CV3 carbonaceous chondrites: constraints on the accretion ages of chondritic asteroids. *Geochim. Cosmochim. Acta* **199**, 58–74.

Jones C. L. and Brearley A. J. (2006) Experimental aqueous alteration of the Allende meteorite under oxidizing conditions: constraints on asteroidal alteration. *Geochim. Cosmochim. Acta* **70**, 1040–1058.

Kakos G. A., Turney T. W. and Williams T. B. (1994) Synthesis and structure of tochilinite: a layered metal hydroxide/sulfide composite. *J. Solid State Chem.* **108**, 102–111.

Kallemeyn G. W. and Wasson J. T. (1981) The compositional classification of chondrites—I. The carbonaceous chondrite groups. *Geochim. Cosmochim. Acta* **45**, 1217–1230.

Karunadasa K. S., Manoratne C. H., Pitawala H. M. T. G. A. and Rajapakse R. M. G. (2019) Thermal decomposition of calcium carbonate (calcite polymorph) as examined by in-situ high-temperature X-ray powder diffraction. *J. Phys. Chem. Solids* **134**, 21–28.

Keller L. P. and Buseck P. R. (1990) Matrix mineralogy of the Lancé CO3 carbonaceous chondrite: A transmission electron microscope study. *Geochim. Cosmochim. Acta* **54**, 1155–1163.

Kikuchi S., Shibuya T., Abe M. and Uematsu K. (2021) Experimental chondrite–water reactions under reducing and low-temperature hydrothermal conditions: Implications for incipient aqueous alteration in planetesimals. *Geochim. Cosmochim. Acta*, doi: 10.1016/j.gca.2021.11.006.

Kimura M., Imae N., Komatsu M., Barrat J. A., Greenwood R. C., Yamaguchi A. and Noguchi T. (2020) The most primitive CM chondrites, Asuka 12085, 12169, and 12236, of subtypes 3.0–2.8: Their characteristic features and classification. *Polar Sci.*, doi: 10.1016/j.polar.2020.100565.

King A. J., Solomon J. R., Schofield P. F. and Russell S. S. (2015) Characterising the CI and CI-like carbonaceous chondrites using thermogravimetric analysis and infrared spectroscopy. *Earth Planets Space* **67**, 1–12.

King A. J., Schofield P. F. and Russell S. S. (2017) Type 1 aqueous alteration in CM carbonaceous chondrites: Implications for the evolution of water-rich asteroids. *Meteorit. Planet. Sci.* **52**, 1197–1215.

King A. J., Bates H. C., Krietsch D., Busemann H., Clay P. L., Schofield P. F. and Russell S. S. (2019) The Yamato-type (CY) carbonaceous chondrite group: Analogues for the surface of asteroid Ryugu? *Geochemistry* **79** 125531.

Kleine T., Budde G., Burkhardt C., Kruijer T. S., Worsham E. A., Morbidelli A. and Nimmo F. (2020) The Non-carbonaceous–Carbonaceous Meteorite Dichotomy. *Space Sci. Rev.* **216**, 1–27.

Krot A. N., Petaev M. I., Scott E. R., Choi B. G., Zolensky M. E. and Keil K. (1998) Progressive alteration in CV3 chondrites: More evidence for asteroidal alteration. *Meteorit. Planet. Sci.* **33**, 1065–1085.

Krot A. N., Petaev M. I. and Bland P. A. (2004) Multiple formation mechanisms of ferrous olivine in CV carbonaceous chondrites during fluid-assisted metamorphism. *Antarc. Met. Res.* **17**, 153–171.

Krot A. N., Hutcheon I. D., Brearley A. J., Pravdivtseva O. V., Petaev M. I. and Hohenberg C. M. (2006) Timescales and settings for alteration of chondritic meteorites. *Meteorit. Early Solar Syst. II*, 525–553.

Lamadrid H. M., Rimstidt J. D., Schwarzenbach E. M., Klein F., Ulrich S., Dolocan A. and Bodnar R. J. (2017) Effect of water activity on rates of serpentinization of olivine. *Nat. Commun.* **8**, 1–9.

Le Guillou C., Changela H. G. and Brearley A. J. (2015) Widespread oxidized and hydrated amorphous silicates in CR chondrites matrices: Implications for alteration conditions and H2 degassing of asteroids. *Earth Planet. Sci. Lett.* **420**, 162–173.

Lee M. R., Lindgren P., Sofe M. R., Alexander C. O. D. and Wang J. (2012) Extended chronologies of aqueous alteration in the CM2 carbonaceous chondrites: Evidence from carbonates in Queen Alexandra Range 93005. *Geochim. Cosmochim. Acta* **92**, 148–169.

Lee M. R., Lindgren P. and Sofe M. R. (2014) Aragonite, breunnerite, calcite and dolomite in the CM carbonaceous chondrites: High fidelity recorders of progressive parent body aqueous alteration. *Geochim. Cosmochim. Acta* **144**, 126–156.

Lee M. R., Cohen B. E. and King A. J. (2019a) Alkali-halogen metasomatism of the CM carbonaceous chondrites. *Meteorit. Planet. Sci.* **54**, 3052–3063.

Lee M. R., Cohen B. E., King A. J. and Greenwood R. C. (2019b) The diversity of CM carbonaceous chondrite parent bodies explored using Lewis Cliff 85311. *Geochim. Cosmochim. Acta* **264**, 224–244.

Leroux H., Cuvillier P., Zanda B. and Hewins R. H. (2015) GEMS-like material in the matrix of the Paris meteorite and the early stages of alteration of CM chondrites. *Geochim. Cosmochim. Acta* **170**, 247–265.

Lindgren P., Lee M. R., Starkey N. A. and Franchi I. A. (2017) Fluid evolution in CM carbonaceous chondrites tracked through the oxygen isotopic compositions of carbonates. *Geochim. Cosmochim. Acta* **204**, 240–251.

MacPherson G. J. and Krot A. N. (2014) The formation of Ca-, Fe-rich silicates in reduced and oxidized CV chondrites: the roles of impact-modified porosity and permeability, and heterogeneous distribution of water ices. *Meteorit. Planet. Sci.* **49**, 1250–1270.

Marrocchi Y., Bekaert D. V. and Piani L. (2018) Origin and abundance of water in carbonaceous asteroids. *Earth Planet. Sci. Lett.* **482**, 23–32.

McAdam M. M., Sunshine J. M., Howard K. T., Alexander C. M., McCoy T. J. and Bus S. J. (2018) Spectral evidence for amorphous silicates in least-processed CO meteorites and their parent bodies. *Icarus* **306**, 32–49.

McSween, Jr, H. Y. (1977a) Petrographic variations among carbonaceous chondrites of the Vigarano type. *Geochim. Cosmochim. Acta* **41**, 1777–1790.

McSween, Jr, H. Y. (1977b) Carbonaceous chondrites of the Ornans type: A metamorphic sequence. *Geochim. Cosmochim. Acta* **41**, 477–491.

Moriarty G. M., Rumble, III, D. and Friedrich J. M. (2009) Compositions of four unusual CM or CM-related Antarctic chondrites. *Geochemistry* **69**, 161–168.

Morris, A. A., (2008). Understanding the origin and evolution of water in the early solar system. (Doctoral dissertation, The Open University). Archive copy only, available at: The Open University Library, First Floor Mobile Shelves, 523.51 MOR.

Nakamura-Messenger K., Clemett S. J., Messenger S. and Keller L. P. (2011) Experimental aqueous alteration of cometary dust. *Meteorit. Planet. Sci.* **46**, 843–856.

Nanne J. A., Nimmo F., Cuzzi J. N. and Kleine T. (2019) Origin of the non-carbonaceous–carbonaceous meteorite dichotomy. *Earth Planet. Sci. Lett.* **511**, 44–54.

Nelson R., Nuth J. A. and Donn B. (1987) A kinetic study of the hydrous alteration of amorphous MgSiO smokes: Implications for cometary particles and chondrite matrix. *J. Geophys. Res. Solid Earth* **92**, 657–662.

Noguchi T., Nakamura T., Ushikubo T., Kita N. T., Valley J. W., Yamanaka R., Kimoto Y. and Kitazawa Y. (2011) A chondrule-like object captured by space-exposed aerogel on the international space station. *Earth Planet. Sci. Lett.* **309**, 198–206.

Noguchi T., Ohashi N., Tsujimoto S., Mitsunari T., Bradley J. P., Nakamura T., Toh S., Stephan T., Iwata N. and Imae N. (2015) Cometary dust in Antarctic ice and snow: Past and present chondritic porous micrometeorites preserved on the Earth's surface. *Earth Planet. Sci. Lett.* **410**, 1–11.

Ohnishi I. and Tomeoka K. (2007) Hydrothermal alteration experiments of enstatite: implications for aqueous alteration of carbonaceous chondrites. *Meteorit. Planet. Sci.* **42**, 49–61.

Olsson-Francis K., Pearson V. K., Steer E. D. and Schwenzer S. P. (2017) Determination of geochemical bio-signatures in mars-like basaltic environments. *Front. Microbiol.* **8**, 1–17.

Palandri J. L. and Reed M. H. (2004) Geochemical models of metasomatism in ultramafic systems: serpentinization, rodingitization, and sea floor carbonate chimney precipitation. *Geochim. Cosmochim. Acta* **68**, 1115–1133.

Palmer E. E. and Lauretta D. S. (2011) Aqueous alteration of kamacite in CM chondrites. *Meteorit. Planet. Sci.* **46**, 1587–1607.

Peng Y. and Jing Y. (2014) Hydrothermal preparation of analogous matrix minerals of CM carbonaceous chondrites from metal alloy particles. *Earth Planet. Sci. Lett.* **408**, 252–262.

Peng Y., Xi G., Zhong C., Wang L., Lu J., Sun X., Zhu L., Han Q., Chen L., Shi L. and Sun M. (2009) An experimental study on the preparation of tochilinite-originated intercalation compounds comprised of $Fe_{1x}S$ host layers and various kinds of guest layers. *Geochim. Cosmochim. Acta* **73**, 4862–4878.

Pignatelli I., Bourdelle F., Bartier D., Mosser-Ruck R., Truche L., Mugnaioli E. and Michau N. (2014) Iron–clay interactions: Detailed study of the mineralogical transformation of claystone

with emphasis on the formation of iron-rich T-O phyllosilicates in a step-by-step cooling experiment from 90 C to 40 C. *Chem. Geol.* **387**, 1–11.

Pignatelli I., Marrocchi Y., Mugnaioli E., Bourdelle F. and Gounelle M. (2017) Mineralogical, crystallographic and redox features of the earliest stages of fluid alteration in CM chondrites. *Geochim. Cosmochim. Acta* **209**, 106–122.

Pourbaix, M., and DeZoubov, N. (1974) Iron. In Atlas of Electrochemical Equilibria in Aqueous Solutions. (ed. M. Pourbaix), 307–321.

Reed M. H. (1982) Calculation of multicomponent chemical equilibria and reaction processes in systems involving minerals, gases and an aqueous phase. *Geochim. Cosmochim. Acta* **46**, 513–528.

Reed M. H. (1983) Seawater-basalt reaction and the origin of greenstones and related ore deposits. *Econ Geol.* **78**, 466–485.

Reed M. H., Spycher N. F. and Palandri J. (2010) *Users Guide for CHIM-XPT: A Program for Computing Reaction Processes in Aqueous-Mineral-Gas Systems and MINTAB Guide*. University of Oregon.

Remusat L., Le Guillou C., Rouzaud J. N., Binet L., Derenne S. and Robert F. (2008) Molecular study of insoluble organic matter in Kainsaz CO3 carbonaceous chondrite: Comparison with CI and CM IOM. *Meteorit. Planet. Sci.* **43**, 1099–1111.

Rietmeijer F. J., Nuth, III, J. A. and Nelson R. N. (2004) Laboratory hydration of condensed magnesiosilica smokes with implications for hydrated silicates in IDPs and comets. *Meteorit. Planet. Sci.* **39**, 723–746.

Rowe M. W., Clayton R. N. and Mayeda T. K. (1994) Oxygen isotopes in separated components of CI and CM meteorites. *Geochim. Cosmochim. Acta* **58**, 5341–5347.

Rubin A. E. (2015) An American on Paris: Extent of aqueous alteration of a CM chondrite and the petrography of its refractory and amoeboid olivine inclusions. *Meteorit. Planet. Sci.* **50**, 1595–1612.

Rubin A. E. and Wasson J. T. (1986) Chondrules in the Murray CM2 meteorite and compositional differences between CM-CO and ordinary chondrite chondrules. *Geochim. Cosmochim. Acta* **50**, 307–315.

Rubin A. E., James J. A., Keck B. D., Weeks K. S., Sears D. W. and Jarosewich E. (1985) The Colony meteorite and variations in CO3 chondrite properties. *Meteoritics* **20**, 175–196.

Rubin A. E., Trigo-Rodríguez J. M., Huber H. and Wasson J. T. (2007) Progressive aqueous alteration of CM carbonaceous chondrites. *Geochim. Cosmochim. Acta* **71**, 2361–2382.

Russell S. S., Huss G. R., Fahey A. J., Greenwood R. C., Hutchison R. and Wasserburg G. J. (1998) An isotopic and petrologic study of calcium-aluminum-rich inclusions from CO3 meteorites. *Geochim. Cosmochim. Acta* **62**, 689–714.

Schikorr G. (1929) Über die reaktionen zwischen eisen, seinen hydroxyden und wasser. *Z. Elektrochem. Angew. Phys. Chem.* **35**, 65–70.

Shipko F. J. and Douglas D. L. (1956) Stability of ferrous hydroxide precipitates. *J. Phys. Chem* **60**, 1519–1523.

Schofield P. F., Knight K. S., Covey-Crump S. J., Cressey G. and Stretton I. C. (2002) Accurate quantification of the modal mineralogy of rocks when image analysis is difficult. *Mineral. Mag.* **66**, 189–200.

Schrader D. L. and Davidson J. (2017) CM and CO chondrites: A common parent body or asteroidal neighbors? Insights from chondrule silicates. *Geochim. Cosmochim. Acta* **214**, 157–171.

Schrader D. L., Davidson J., McCoy T. J., Zega T. J., Russell S. S., Domanik K. J. and King A. J. (2021) The Fe/S ratio of pyrrhotite group sulfides in chondrites: An indicator of oxidation and implications for return samples from asteroids Ryugu and Bennu. *Geochim. Cosmochim. Acta* **303**, 66–91.

Schwenzer S. P. and Kring D. A. (2013) Alteration minerals in impact-generated hydrothermal systems - Exploring host rock variability. *Icarus* **226**, 487–496.

Scott E. R. and Jones R. H. (1990) Disentangling nebular and asteroidal features of C03 carbonaceous chondrite meteorites. *Geochim. Cosmochim. Acta* **54**, 2485–2502.

Sears D. W., Batchelor J. D., Lu J. and Keck B. D. (1991) Metamorphism of CO and CO-like chondrites and comparisons with type 3 ordinary chondrites. *Antar. Met. Res.* **4**, 319–343.

Shukolyukov A. and Lugmair G. W. (2002) Chronology of asteroid accretion and differentiation. *Asteroids* **III**, 687–695.

Siriwardane R. V., Poston, Jr, J. A., Fisher E. P., Shen M. S. and Miltz A. L. (1999) Decomposition of the sulfates of copper, iron (II), iron (III), nickel, and zinc: XPS, SEM, DRIFTS, XRD, and TGA study. *Appl. Surf. Sci.* **152**, 219–236.

Sugiura N. and Fujiya W. (2014) Correlated accretion ages and ε^{54}Cr of meteorite parent bodies and the evolution of the solar nebula. *Meteorit. Planet. Sci.* **49**, 772–787.

Suttle M. D., King A. J., Schofield P. F. and Russell S. S. (2021a) The aqueous alteration of CM chondrites, a review. *Geochim. Cosmochim. Acta* **299**, 219–256.

Suttle M. D., Folco L., Genge M. J., Franchi I. A., Campanale F., Mugnaioli E. and Zhao X. (2021b) The aqueous alteration of GEMS-like amorphous silicate in a chondritic micrometeorite by Antarctic water. *Geochim. Cosmochim. Acta* **293**, 399–421.

Takigawa A., Furukawa Y., Kimura Y., Davidsson B. and Nakamura T. (2019) Exposure experiments of amorphous silicates and organics to cometary ice and vapour analogs. *Astrophys. J.* **881**.

The Meteoritical Bulletin (2021), online and available at: https://www.lpi.usra.edu/meteor/ (accessed on 09/07/2021).

Telus M., Hauri E. H. and Wang J. (2019) Calcite and dolomite formation in the CM parent body: Insight from in situ C and O isotope analyses. *Geochim. Cosmochim. Acta* **260**, 275–291.

Tomeoka K. and Itoh D. (2004) Sodium-metasomatism in chondrules in CO3 chondrites: Relationship to parent body thermal metamorphism. *Meteorit. Planet. Sci.* **39**, 1359–1373.

Torrano Z. A., Schrader D. L., Davidson J., Greenwood R. C., Dunlap D. R. and Wadhwa M. (2021) The relationship between CM and CO chondrites: Insights from combined analyses of titanium, chromium, and oxygen isotopes in CM, CO, and ungrouped chondrites. *Geochim. Cosmochim. Acta* **301**, 70–90.

Tyra M., Brearley A. and Guan Y. (2016) Episodic carbonate precipitation in the CM chondrite ALH 84049: An ion microprobe analysis of O and C isotopes. *Geochim. Cosmochim. Acta* **175**, 195–207.

Vacher L. G., Marrocchi Y., Villeneuve J., Verdier-Paoletti M. J. and Gounelle M. (2017) Petrographic and C & O isotopic characteristics of the earliest stages of aqueous alteration of CM chondrites. *Geochim. Cosmochim. Acta* **213**, 271–290.

Vacher L. G., Piralla M., Gounelle M., Bizzarro M. and Marrocchi Y. (2019a) Thermal evolution of hydrated asteroids inferred from oxygen isotopes. *Astrophys. J. Lett.* **882**, L20.

Vacher L. G., Truche L., Faure F., Tissandier L., Mosser-Ruck R. and Marrocchi Y. (2019b) Deciphering the conditions of tochilinite and cronstedtite formation in CM chondrites from low temperature hydrothermal experiments. *Meteorit. Planet. Sci.* **54**, 1870–1889.

Verdier-Paoletti M. J., Marrocchi Y., Avice G., Roskosz M., Gurenko A. and Gounelle M. (2017) Oxygen isotope constraints on the alteration temperatures of CM chondrites. *Earth Planet. Sci. Lett.* **458**, 273–281.

Visser R., John T., Whitehouse M. J., Patzek M. and Bischoff A. (2020) A short-lived 26Al induced hydrothermal alteration event in the outer solar system: Constraints from Mn/Cr ages of carbonates. *Earth Planet. Sci. Lett.* **547** 116440.

Warren P. H. (2011) Stable-isotopic anomalies and the accretionary assemblage of the Earth and Mars: A subordinate role for carbonaceous chondrites. *Earth Planet. Sci. Lett.* **311**, 93–100.

Weisberg, M.K., McCoy, T.J. and Krot, A.N., (2006). Systematics and evaluation of meteorite classification. *Meteorit. Early Solar Syst. II*, 19–52.

Yapp C. J. (1990) Oxygen isotopes in iron (III) oxides: 1. Mineral-water fractionation factors. *Chem. Geol.* **85**, 329–335.

Yong-fei Z. (1991) Calculation of oxygen isotope fractionation in metal oxides. *Geochim. Cosmochim. Acta* **55**, 2299–2307.

Young E. D. (2001) The hydrology of carbonaceous chondrite parent bodies and the evolution of planet progenitors. *Philos. Trans. Royal Soc. A* **359**, 2095–2110.

Young E. D., Ash R. D., England P. and Rumble D. (1999) Fluid flow in chondritic parent bodies: Deciphering the compositions of planetesimals. *Science* **286**, 1331–1335.

Yurimoto H., Krot A. N., Choi B. G., Aléon J., Kunihiro T. and Brearley A. J. (2008) Oxygen isotopes of chondritic components. *Rev. Mineral Geochem.* **68**, 141–186.

Zhu K., Moynier F., Schiller M., Alexander C. M. D., Davidson J., Schrader D. L., van Kooten E. and Bizzarro M. (2021) Chromium isotopic insights into the origin of chondrite parent bodies and the early terrestrial volatile depletion. *Geochim. Cosmochim. Acta* **301**, 158–186.

Zega T. J., Garvie L. A., Dódony I., Friedrich H., Stroud R. M. and Buseck P. R. (2006) Polyhedral serpentine grains in CM chondrites. *Meteorit. Planet. Sci.* **41**, 681–688.

Zolotov M. Y., Mironenko M. V. and Shock E. L. (2006) Thermodynamic constraints on fayalite formation on parent bodies of chondrites. *Meteorit. Planet. Sci.* **41**, 1775–1796.

Associate editor: Yves Marrocchi